Injectable Peptide-Based Biomaterials for Cell Delivery

Jinane El Hage

Thesis submitted to the University of Ottawa in fulfillment of the requirements for the MSc in Biochemistry

Department of Biochemistry, Microbiology, and Immunology (BCH)
Faculty of Medicine
University of Ottawa

In honor of my grandparents,
Dr. Mohsen and Dr. Hikmat El Hage,
Thanks for being my inspiration.

Abstract

Keratoconus is a progressive degenerative corneal disease characterized by stromal thinning and ectasia, often leading to significant visual impairment. Injectable biomaterials offer a promising minimally invasive alternative to corneal transplantation by reinforcing stromal structure and delivering therapeutic agents directly to the site of damage. This thesis focuses on the development, optimization, and characterization of collagen-like peptide (CLP)-based hydrogel microspheres as a platform for cell encapsulation and delivery in Keratoconus treatment. Building on previous work that demonstrated the efficacy of CLPs in forming on-the-spot hydrogels for tissue repair, this study adapts the formulation to a microfluidic platform for generating monodisperse microspheres suitable for cell delivery.

A library of CLP sequences was screened with some sequences optimized to fit the current applications. C30 collagen-like peptide emerged as the optimal candidate due to its biocompatibility, gelation properties, and consistent microsphere formation. Microfluidic encapsulation parameters were optimized to ensure uniform sphere morphology and high cell viability. Live/dead assays demonstrated sustained viability of encapsulated GFP+ fibroblast cells over 72 hours, with C30 microspheres outperforming agarose controls in long-term cell survival. Scanning electron microscopy and pore size distribution analysis confirmed a porous architecture suitable for nutrient and waste exchange. Additional physicochemical characterizations, including circular dichroism, differential scanning calorimetry, rheology, and infrared spectroscopy, validated the structural stability and peptide nature of the materials.

Together, these findings highlight the potential of CLP-based microspheres as a novel injectable platform for targeted and biocompatible therapeutic delivery to the cornea, supporting future development of minimally invasive regenerative treatments for Keratoconus.

Acknowledgements

First and foremost, I want to thank my professor, Dr. Emilio I. Alarcón, for giving me more opportunities than I knew what to do with. With him, opportunities weren't just about experiments and publications; they were about growing as a person just as much as growing as a scientist. And for that, I am grateful. You opened doors I didn't even know existed, let me wander and dream, but also brought me back to earth when necessary. You believed in me, challenged me, and made this experience feel like home. Without you, my graduate journey would have looked very different, and I am thankful for the one I got to live.

To the members of the Alarcón Lab, I would like to begin by thanking Dr. David Garcia Shejtman, with whom I've spent countless lunch hours geeking out over music, movies, and TV series, diving into every plot twist and fan theory imaginable. You are the source of my unexpected crash course in pop culture, and the person who made peptide chemistry somehow fun. Your knowledge in the field is truly remarkable, but beyond that, your kindness and support took this project to another level. Thank you for helping me navigate what I didn't know and for making what I did know feel more complete. Thank you to Dr. Juan David, Dr. Irene Guzman Soto, Jessica Hernandez, Julie Da Silva, Deyanira Hernandez, and Ramis Ileri for your direct or indirect contributions to this project, but more importantly, for the countless moments that made long lab days more bearable. We shared much more than lab benches and lunch hours, thank you for that. A special shoutout to Andres Mercado, who supported me from the very beginning, through all the rough patches when nothing was working, and who celebrated my wins when things finally did. Thank you for your patience, for teaching me the joys (and pains) of peptide chemistry, and for walking me through experiments that I otherwise would have absolutely struggled with.

To Dr. Michael Godin and his team, thank you for welcoming me as one of your own. A special thanks to Nicholas Soucy, whose engineering expertise and microfluidic wizardry kept me from losing my mind.

My support system starts at home. Mom and Dad, Rowaida and Samir, thank you for believing in me, even when you kept joking that I was secretly working on a biological weapon. Your unwavering support (and occasional skepticism) made this journey possible.

To my friends, more like family by choice, who stood by me through it all, MJ, AM, JB, DC, KA, FA, RM and AS. You kept me going when I lost belief in myself. Even if you didn't quite understand what a peptide was, the fact that you cared meant everything to me.

BZ, where do I even begin? Your unwavering support during some of the hardest times never went unnoticed. Everything feels easier with you by my side. Writing this acknowledgment is difficult because words will never truly capture all that you have done for me and everything we have been through together. Thank you for always being by my side and never letting my own doubts get to me.

Finally, to the University of Ottawa Heart Institute team, thank you for fostering an environment where researchers have the freedom, support, and resources to turn their ideas into reality.

This journey wasn't always easy, but it was never lonely. For that, I am grateful.

Table of Contents

List of Abbreviations

ADSC – Adipose derived adult stem cells

AMA – Allyl methacrylate

ATR – Attenuated total reflectance

CD – Circular Dichroism

CEPS – Corneal epithelial cell sheets

CLP – Collagen-like-peptide

CO2 – Carbon dioxide

Cryo-SEM – Scanning electron cryo-microscopy

CS – Chitosan

CXL – Crosslinking

DMEM – Dulbecco's modified eagle medium

DMSO – Dimethyl sulfoxide

DNA – Deoxyribonucleic acid

DOG – Disulfide oxidation glycine

DSC – Differential scanning calorimetry

ECM – Extracellular matrix

EDTA – Ethylenediaminetetraacetic acid

EGDMA – Ethylene glycol dimethacrylate

FBC – Fibroblast cells

FBS – Fetal bovine serum

FDA – Food and drug administration

FTIR – Fourier-transform infrared

GCG – Glycine-Cysteine-Glycine

GFP-FBCs – Green fluorescent protein tagged fibroblast cells

GPP – Glycine-Proline-Proline

GPO – Glycine-Proline-Hydroxyproline

HA – Hyaluronic acid

HEMA – 2-Hydroxyethyl methacrylate

HFBCs – Human fibroblast cells

HLB – Hydrophilic–lipophilic balance

ICRS – Intracorneal ring segments

IR – Infrared

KV – Kilovolt

LSCD – Limbal stem-cell deficiency

MES – 2-(N-morpholino) ethanesulfonic acid

MI – Myocardial infarction

MMP – Matrix metalloprotease

MSC – Mesenchymal stem cells

NH – Nitrogen hydride

NH2 – Amine group

OH – Hydroxyl group

PBS – Phosphate buffer saline

PCL – Polycaprolactone

PDMS – Poly(dimethylsiloxane)

PEG-Mal – 8-arm Polyethylene glycol with Maleimide groups flanked on each arm

PEO – Polyethylene oxide

PEEK – Polyether Ether Ketone

PGA – Polyglycolic acid

PLA – Polylactic acid

PLGA – Poly (lactic-co-glycolic acid)

PU – Polyurethane

PVA – Polyvinyl alcohol

W/O – Water in oil emulsion

List of Figures/Tables/Schemes

Introduction

1.1 Keratoconus: Pathophysiology and Challenges

Corneal diseases and the quality of life

Corneal diseases, particularly Keratoconus, significantly impact patients' quality of life[1]. The cornea, the transparent outer structure of the eye, plays a crucial role in vision by focusing light onto the retina[2,3]. It consists of five layers: the epithelium, Bowman's layer, the stroma, Descemet's membrane, and the endothelium[4,5]. Each layer has specific functions, the epithelium is a layer of cells covering the cornea's surface and helps protect it from damage, Bowman's layer is a thin layer of collagen fibers that provides structural support to the cornea, the stroma is the thickest layer made up of water and collagen and is responsible for its refractive properties, Descemet's membrane is a thin layer of collagen fibers that separates the stroma from endothelium, and the endothelium is a single layer of cells that helps maintain the cornea's clarity by pumping excess fluid out of the cornea [6,7]. Therefore, any damage to the corneal structure or its transparency contributes to vision loss.

Corneal blindness is the fourth most common form of blindness globally, affecting 23 million people and imposing a significant economic and social burden[8,9]. Keratoconus, a bilateral and usually asymmetrical ectatic corneal disease, affects approximately 21 per 1000 men and 18 per 1000 women with an overall reported prevalence of 54.5 per 100,000 with some recent studies showing an even higher prevalence of 0.2-0.3 % in the general population[10–13]. It is characterized by progressive thinning and bulging of the cornea into an irregular cone shape, leading to astigmatism and severe vision decline over time, ultimately resulting in vision loss[14].

The onset of Keratoconus usually occurs in puberty or early adulthood, continuing into prime earning and child-rearing years, representing a substantial public health burden. Over an average disease duration of 37 years, the cost of care for a person with Keratoconus is $24,168 more than for a person with myopia, with significant expenses for surgical procedures and regular ophthalmologic care [15]. In the US and Canada, the lifetime cost of treatment for Keratoconus in 2019 was nearly $29,000 per person, with a cumulative economic burden of $3.8 billion[16–18].

The exact etiology of Keratoconus is unknown, but it is believed to result from a combination of hereditary, genetic, and environmental factors including Down syndrome, Ehlers-Danlos syndrome, eye rubbing, ultraviolet exposure, allergic diseases, or specific diseases and inflammation [14,19–21] .

Biochemical and Structural Changes in Keratoconus Corneas

Keratoconus involves significant biochemical and structural changes in the cornea, primarily the degradation of collagen fibers and reduction in the number of keratocytes, mainly in the stroma [22]. It is also associated with fewer lamellae and deterioration of fibroblasts [23]. Researchers have observed different patterns in the overall arrangement of collagen lamellae and an irregular distribution of collagen fibril mass, particularly near the cone's apex in Keratoconus-affected corneas compared to normal corneas [24].

Collagen is essential for maintaining the cornea's strength and flexibility, helping to keep its regular round shape[25,26]. In Keratoconus, an imbalance in matrix metalloproteases (MMPs), a family of zinc-dependent proteases, has been studied[22]. These enzymes are involved in the degradation and remodeling of the extracellular matrix (ECM) proteins, which are important components of the cornea[27]. Some studies suggest that MMPs may contribute to the development of Keratoconus by disturbing the balance between ECM synthesis and degradation, leading to corneal thinning and weakening[28]. Additionally, other research indicates that keratocytes, specialized cells in the cornea responsible for preserving its structure and function, may also play a role in Keratoconus pathogenesis[29]. This is demonstrated by the loss of keratocytes due to abnormal apoptosis, which contributes to corneal thinning and weakening[29].

1.2 Current Treatment Landscape and Unmet Needs in Keratoconus

Current Approaches for Managing Keratoconus

In the early stages of Keratoconus, glasses or contact lenses are used to provide better vision correction and improved acuity[30]. For example, scleral contact lenses are designed to vault over the entire cornea surface and rest on the sclera (the white part of the eye) without touching

the cornea directly. Since scleral contacts place all their weight on the sclera, they avoid the highly innervated cornea which improves comfort. Another type of contact lenses is the Rigid Gas Permeable (RGP) contact lens, which is a hard plastic lens that act as the eye's second surface, compensating for curvature irregularities and helping retain the corneal shape and position in the eye. Intracorneal ring segments, *e.g.*, US FDA-approved Intacs ®, have also been introduced as a minimally invasive procedure in which small arc-shaped implants made of synthetic material, typically polymethyl methacrylate, are implanted within the corneal stroma to induce a geometry change, improve its refractive properties, and confer a centrally flattening effect in Keratoconus patients[31–33]. Unfortunately, later disease stages are rarely improved by contact lenses and instead show improvement following corneal collagen crosslinking (CXL) treatments[34,35]. This approach involves the formation of bonds between collagen molecules, fibers and microfibrils, which can stabilize corneal thickness and the remaining collagen fibers, postponing further degradation by the disease[36–38]. In its basic form, the procedure works by applying a photosensitizer, riboflavin, on the cornea followed by its activation by shining a UV-A light. Exposing riboflavin to UV-A light leads to the generation of reactive oxygen species (ROS) that crosslinks the collagen fibers in the cornea by forming covalent bonds between collagen molecules and between collagen molecules and proteoglycans in the ECM [36,39]. When the cornea is severely damaged from Keratoconus and no longer responds to the other treatments like corneal collagen crosslinking, corneal transplantation (keratoplasty) becomes the only viable option[34].

Limitations of Current Keratoconus Treatments

There have been significant advancements in the management of Keratoconus, several limitations remain with the current treatment options. Scleral contact lenses are very costly, collect debris, need cleaning during the day, and require special training for fitting [40]. Other contact lenses like RGP can be uncomfortable for some patients and require prescription glasses over the contacts to obtain optimized vision. They can also lead to dryness symptoms, irritation in dusty environments, and aggravate corneal irregularities, possibly making the cornea cloudy in patients under 20 years of age [41].

While intracorneal ring segments (ICRS) have shown some benefits in managing early stages of Keratoconus, they come with many complications such as corneal perforation, infectious

keratitis, broken ring segments, ring exposure or extrusion, corneal melting, and vascularization [42,43]. There have also been variable visual outcomes, with approximately 1 in 3 patients not experiencing satisfactory visual improvement following ICRS implantation. It may not be effective for all patients and has unpredictable refractive results with variable long-term outcomes in terms of stability and regression [33,44,45].

For corneal collagen crosslinking, while this technique is widely used for Keratoconus and has been effective in some cases to slow or halt disease progression, it is not a cure or long-term solution. It may not fully restore the corneal shape or visual acuity in all patients, and generally only stabilizes the remaining collagen in the already thinned corneas instead of replacing the lost collagenous ECM. It is also not suitable for individuals with advanced stages of the disease, where the cornea is often too thin to repair safely with increasing the risk of UV-A light penetrating deeper into the eye and potentially damaging the endothelium or other intraocular structures [46].

Finally, corneal transplantation, or keratoplasty, has shown great success, but is inaccessible to 53% of the population[8,9]. Today, it is estimated that 12.7 million people are currently awaiting a donor cornea, with only 1 cornea available for every 70 needed due to a shortage in cornea donors[8,9]. The surgery can also lead to complications including severe postoperative astigmatism, delayed visual rehabilitation, and graft rejection [47,48].

Despite the advancements of these approaches, their focus is mainly on managing symptoms instead of addressing the underlying pathology or restoring corneal structure. These gaps highlight the pressing need to develop therapeutic alternatives to corneal transplantation, including regenerative approaches that encompass cell-based therapy and bioengineered constructs like corneal implants, which offer promising alternatives by aiming to regenerate damaged tissue and improve long-term outcomes. Such strategies have the potential to bridge the gaps in current treatments, providing more effective and sustainable solutions for patients suffering from corneal diseases. This leads us to explore the role of biomaterials in corneal tissue repair, which is the focus of the next section.

1.3 The Role of Biomaterials in Cornea Tissue Repair

Biomaterials, designed to interact with biological systems to repair, replace, or regenerate damaged tissues, have been widely used in corneal tissue repair and regeneration. These materials can be natural, synthetics, or hybrid. In ophthalmology, biomaterials are classified based on their composition and application [49].

Early Ophthalmic Applications of Biomaterials

The earliest and most well-known ophthalmic biomaterials are contact lenses, currently composed of hydrogel and silicone hydrogel [49–51]. Various types of biomaterials have been developed for contact lenses, but those that stand out are made with stable polymers that can absorb or bind water and include polymeric pores to allow liquid penetration, oxygen, and ion permeability [49]. Other early ophthalmic applications of biomaterials include intraocular lenses, usually composed of acrylics or silicone copolymers, or artificial tears, which contain biomaterials such as hyaluronic acid, dextran, and polyethylene glycol to aid in eye lubrication and increase on-eye retention time [49].

As research progressed and more corneal defects were studied, new biomaterial inventions emerged. In recent decades, hydrogels have gained significant attention for their use in various medical and non-medical applications [52,53]. In biomedical applications, their use in research applications have been identified in tissue engineering, wound healing, and drug delivery systems[54]. Hydrogels are defined as three-dimensional (3D) networks of crosslinked polymer chains capable of absorbing large volumes of water and with tunable properties to improve their biocompatibility, hydrophilicity and mechanical strength, making them ideal for biomedical applications [55].

Hydrogels are particularly interesting in corneal applications due to their injectability, easy tunability (biocompatibility, biodegradability, mechanical strength, hydrophilicity, absorbency, and viscoelasticity), and ability to mimic the cornea's natural environment [56]. As biphasic materials containing at least 10% water, either by weight or volume, they closely resemble natural tissues in elasticity and softness [57]. Soft contact lenses, for instance, are a common application of hydrogels

often made from synthetic polymers such as allyl methacrylate (AMA), ethylene glycol dimethacrylate (EGDMA), and 2-hydroxyethyl methacrylate (HEMA) [49,58]. Hydrogels, like any biomaterials, can be derived from either natural polymers, or synthetic counterparts both of which are used to develop scaffolds that support cell growth and tissue regeneration— making them ideal for corneal repair[52].

Natural vs. Synthetic Biomaterials

Biomaterials used in regenerative medicine can be categorized as either natural or synthetic. Naturally derived biomaterials, including collagen, gelatin, silk fibroin (SF), alginate, chitosan (CS), hyaluronic acid (HA), cellulose and decellularized porcine corneas offer inherent biocompatibility due to the presence of natural extracellular matrix motifs [59]. However, their use is often limited by a poorly-defined composition, lack of precise chemical tunability, batch-to-batch variability, generally weak mechanical properties, and the risk of immunogenicity stemming from biological impurities or pathogen transmission [60,61]. Their limited tunability also makes natural biomaterials unsuitable for personalized treatments, as they are often applied in a uniform, "one-size-fits-all" concept. This approach fails to account for the inherent chemical and physical differences among tissues and organs, as well as individual variations in defect size and tissue structure [62]. Therefore, synthetic biomaterials, or even hybrid systems that combine natural and synthetic components, have gained considerable attention in recent years due to their high scalability, reproducibility, and ability to fine tune their properties for specific applications [63,64]. For example, Gelatin Methacryloyl (GelMA), is a widely used hybrid hydrogel that combines the benefit of natural gelatin with its biocompatibility and cell recognition sites with the mechanical tunability and crosslinking control offered by the synthetic methacrylate functionalization[65]. Among the most widely studied degradable synthetic polymers are Poly(α-hydroxy esters) such as polycaprolactone (PCL), polyglycolic acid (PGA), polylactic acid (PLA), and their copolymer poly (lactic-co-glycolic acid) (PLGA), as well as poly(ethers) like polyethylene oxide (PEO), polyethylene glycol (PEG), polyvinyl alcohol (PVA), and polyurethane (PU) [52,59,66].

The design of an optimal biomaterial for corneal repair must account for several critical properties. Corneal regeneration materials should be biocompatible, transparent, mechanically robust, and moisture resistant [67]. Biocompatibility ensures that the material does not elicit adverse

immune responses or tissue rejection upon contact with ocular tissues [67]. Transparency is essential for preserving the optical clarity necessary for vision [52]. Mechanical properties, including strength and flexibility, are crucial for withstanding the physical stresses exerted on the cornea from blinking while maintaining corneal integrity [68]. Additionally, permeability plays a vital role in facilitating nutrient diffusion while preventing pathogen infiltration, which can be achieved through careful optimization of hydrogel pore size [69]. Depending on the application, certain scaffolds must also promote cell migration, adhesion, differentiation, and proliferation to support tissue regeneration [70–72].

1.4 Peptide-Based Hydrogels for Corneal Regeneration

More recent developments in peptide-based hydrogels have opened new avenues for corneal regeneration ophthalmic applications due to the reasons previously mentioned, making them ideal for mimicking the native corneal extracellular matrix (ECM) [73]. Their ability to self-assemble into three-dimensional networks provides structural support while promoting cell adhesion, migration, and proliferation [55]. Additionally, peptide-based hydrogels can be functionalized with bioactive molecules, such as growth factors or signaling peptides, to enhance regenerative outcomes [74–76]. Their transparency and mechanical properties can be tailored to match the optical and structural requirements of the cornea, ensuring optimal integration and functionality [73]. Synthetic peptide-based hydrogels offer further advantages over natural ones due to their consistent manufacturing, scalability, cost-effectiveness, lack of zoonotic transmission of disease, and specificity [63,64].

With collagen making up seventy percent of the cornea's weight, predominantly in the stromal layer, it stands out as an excellent scaffold material for corneal regeneration, especially in hydrogel form [66,77]. However, animal-derived collagen exhibits certain limitations such as inadequate light transmission, potential immunogenicity, risk of zoonotic transmission of disease, and susceptibility to enzymatic degradation [66]. To overcome these challenges, synthetic collagen-like peptides offer a better alternative as they are designed to mimic the structure and function of natural collagen consistently, cost-effectively, without risks. Among synthetic options, short peptide-based materials (composed of fewer than 50 amino acids) offer distinct advantages [78,79].

These materials can replicate the biological functions of larger proteins, undergo chemical modifications (e.g., to form β-sheet structures that promote self-assemble), and are cost-effective for clinical applications [78,79]. However, achieving robust three-dimensional peptide structures often requires the use of potentially harmful chemical crosslinkers, such as carbodiimide or polymerization catalysts, which can hinder cellular regeneration [80–82]. Therefore, it is common practice to utilize pre-crosslinked materials – free of harmful by-products – before implantation [83]. Additionally, designing peptide sequences to facilitate supramolecular self-assembly after crosslinking is critical for enhancing the material's mechanical properties. One approach involves the bio-orthogonal assembly of peptide hydrogels using cysteine-containing peptides [84–86]. Another strategy conjugates PEG-maleimide (PEG-Mal) with collagen-like peptides (CLPs) via a short cysteine linker to fabricate corneal implants [87]. CLPs, which mimics the tertiary structure of collagen—a protein vital for tissue strength—commonly consist of repeating Glycine-Proline-Proline (GPP) or Glycine-Proline-Hydroxyproline (GPO) triplets[88]. These peptides are typically synthesized using solid-phase peptide synthesis, where peptides are assembled step-by-step on a solid support, enabling precise control over the peptide sequence and structure, to create collagen mimetics with tailored properties [89].

Over a decade ago, Per Fagerholm and colleagues developed a biosynthetic cornea mimic using recombinant human collagen type III (RHC III) synthesized in yeast, chemically cross-linked and molded [90]. The subsequent clinical study implanted these corneal mimics in 10 patients with Keratoconus, demonstrating successful corneal re-epithelialization, nerve regeneration and touch sensitivity restoration, indicating the potential of biosynthetic mimics in facilitating endogenous tissue regeneration [90]. This success spurred further optimization of biosynthetic corneal implants. More recently, Christopher D. McTiernan *et al*., developed LiQD Cornea, a regeneration stimulating liquid corneal replacement, composed of short collagen-like peptides, polyethylene glycol, and fibrinogen [91]. This self-assembling synthetic collagen analog is cost-effective, immune-compatible, and gels at body temperature within five minutes. Since this can be injected in liquid form and solidifies in situ, this approach offers a promising solution for corneal blindness and perforation repair, addressing the current shortage of cornea donors. Another example involves peptide nanofiber scaffolds formed by self-assembling peptide amphiphile

molecules, functionalized with bioactive laminin-derived YIGSR and fibronectin RGD peptides, to enhance corneal regeneration [92].

In the Alarcon lab, our team has developed a multipurpose, fast-gelling peptide hydrogel using a low-volume, rapid-screening approach to identify self-assembling peptide structures with tunable mechanical properties ranging from 1 to 100 kPa in strength [93]. The identifiable peptides consist of short amino acid sequences forming synthetic triple-helical folding collagen-like structures with repetitive POG sequences featuring glycine-flanked cysteine residues at both termini. The reason for flanking cysteine residues with two flexible glycine residues is to allow the sulfhydryl group to move in space[94]. A multi-armed polyethylene glycol (PEG) molecule, a synthetic polymer approved by the FDA for its safety and stability, serves as the polymeric backbone in this design with a maleimide group at each end of its 8 arms to enhance PEG's reactivity and facilitate polymeric network formation[95,96]. Using click chemistry, and at physiological pH, a Michael-Nucleophilic Addition reaction between maleimide and sulfhydryl groups enables the rapid formation of three-dimensional adhesive structures with tunable mechanical characteristics [97] (**Figure 1**). This design leverages two naturally occurring mechanisms to provide tissues with mechanical stability—chemical bonding and molecular self-assembly [97]. The resulting hydrogel forms stable bonds that can last for over two years while minimizing undesired cross-reactions during in vivo applications, unlike other chemical groups such as acrylamides [98,99].

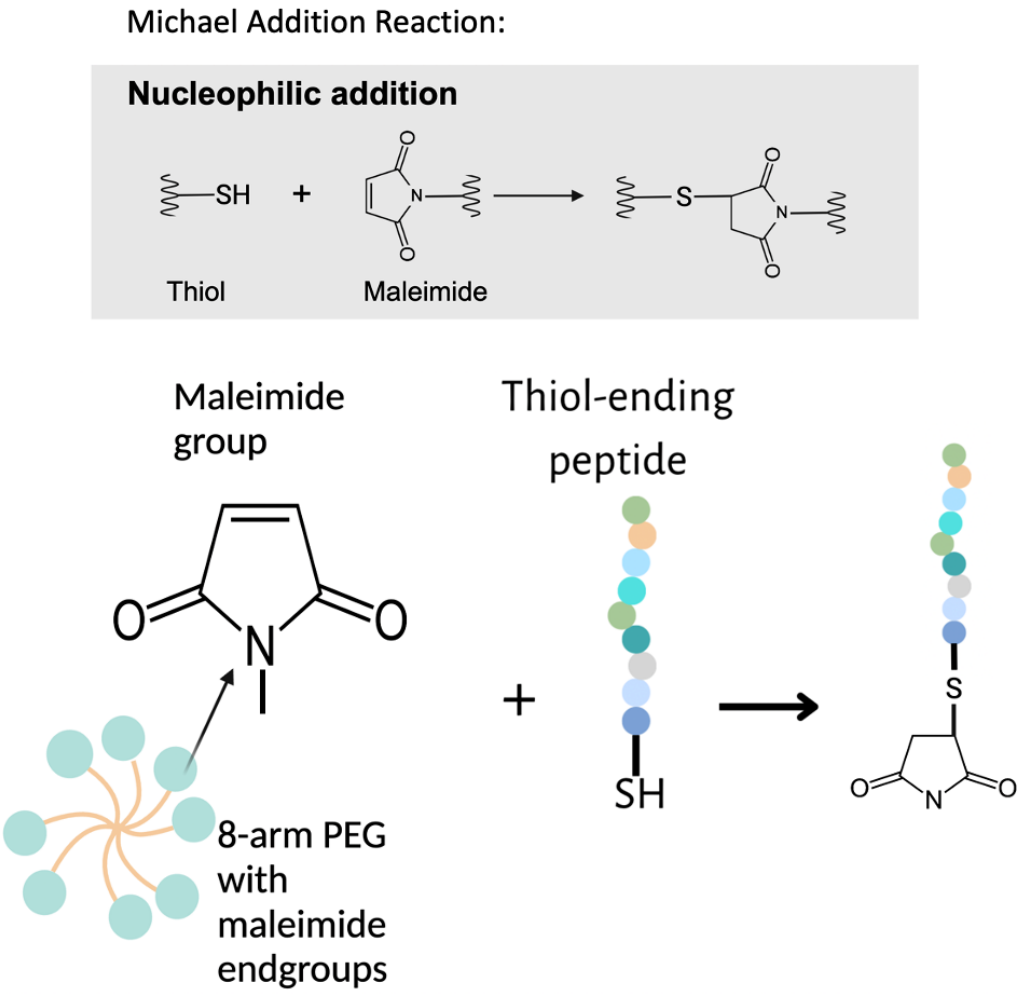

Figure 1. Schematic representation of the Michael addition reaction between a thiol-ending peptide and an 8-arm PEG with maleimide end groups. The reaction involves the nucleophilic addition of the thiol group to the maleimide group, resulting in a stable thioether bond. This process is utilized to functionalize collagen-like peptides for various biomedical applications.

1.5 Cell Therapies in Keratoconus Applications

Several studies have revealed that the culprit of Keratoconus pathogenesis has been linked to the loss of keratocytes and excessive degradation of collagen fibers by matrix metalloproteinases [100,101]. This has led researchers to explore cellular therapies as a novel approach to replace and increase the number of keratocytes and improve their function as these cells are critical for

maintaining corneal structure, producing collagen and extracellular matrix components, and regulating wound healing and transparency[102]. Many studies have focused on cell-based therapies for corneal regeneration, with the goal of replacing or reviving corneal cells directly. These therapies have emerged as potential treatments for various corneal defects [102,103]. Recently, for example, a group in Japan reported the world's first use of corneal epithelial cell sheets derived from human induced pluripotent stem cells (iPSCs) to treat limbal stem-cell deficiency (LSCD), which is a hard-to-treat condition of the loss of corneal epithelial stem cells from the limbus at the edge of the cornea and has severe consequences for vision [104]. This procedure, which involved grafting iPSC-derived corneal epithelial cell sheets (iCEPS) onto the ocular surface after removing fibrotic tissue, showed success and minimal adverse events for two years postoperatively in all four operated eyes.

While still in its early stages, some studies have suggested the potential of cell therapies for corneal stromal regeneration in the context of Keratoconus. For example, studies in animal models showed that intrastromal injection of human keratocytes in animal models has led to an increase in the number of stromal cells and improved their function [105–108]. However, certain challenges remain, such as the propagation of keratocytes in vitro, the need for numerous growth factors in cell culture, the difficulty in obtaining sufficient quantities of cells for tissue engineering, and the immune system response to new cells[109]. Immunological rejection is a common complication in allogenic corneal transplants, especially in cases of repeated transplants or corneal scarring in vascularized corneas. One potential solution involves using non-immunogenic corneas, such as allogenic decellularized corneal scaffolds, which have had their cellular components and genetic material removed[109]. This approach may offer a viable alternative for Keratoconus patients.

Two groups explore the use of stem cells for intrastromal transplantation in Keratoconus patients in clinical trials. The very first Keratoconus cell therapy study was performed by Alio and colleagues in 2017, which set precedence for further research [110,111]. In 2017, Alio *et al.*, conducted a phase 1 trial, which demonstrated the safety and efficacy of implanting adipose-derived adult stem cells (ADSCs) in the corneal stroma of patients with advanced Keratoconus. The outcomes of this study included full transparency of the cornea after 24 hours, improved corneal central thickness and visual acuity, and no intraoperative or postoperative complications [110]. In 2023, Alio

et al., and Ramin *et al.* conducted similar studies, both using autologous ADSCs and employing immunosuppressive treatments or surgically replacing patient's corneas with decellularized corneas to prevent immune rejection before ADSCs implantation[112,113]. Both studies observed no adverse events with improvements in visual acuity and corneal thickness.

Despite these promising results, several challenges remain in cell transplantation therapies. While the studies were effective in most patients, they had little effect in some of them. Additionally, it seems that transplanting cells along may not be sufficient to significantly alter corneal refractive parameters. It is also unclear how many transplanted cells will ultimately remain in the stromal pocket long enough to differentiate and contribute to tissue regeneration. On a similar note, the exact amount of collagen renewal required to regenerate thin and Keratoconic/pathological corneas remains uncertain. Researchers have also attempted various methods to prevent immune reaction, such as using immunosuppressive drugs or fully replacing the cornea with decellularized tissue, but these approaches remain invasive.

From here, we can of think of combining both cellular therapies and tissue engineering approaches as they may, together, offer a promising solution to enhance the outcomes of cell-based treatments for Keratoconus. Biomaterials, particularly hydrogels, can be engineered to protect sensitive cells from shear stress during injection into the corneal stroma, and various bioactive motifs can be added to improve cell adhesion, retention, differentiation, and immune modulation [114,115]. These biomaterials could replace lost collagen tissue, maintain corneal curvature, and provide a supportive environment for cellular regeneration, all while gradually degrading to allow for natural tissue healing [66]. This approach aligns with our study's novel contribution building on our previous work with developing a multipurpose fast-gelling peptide hydrogel that has shown promising results in porcine corneas for thickening and preserving corneal curvature [93]. By combining cellular therapies with biomaterial-based tissue engineering, we aim to create a regenerative strategy that can improve corneal healing and may ultimately extend to other organ and tissue applications. However, this thesis focuses specifically on its potential for corneal stromal regeneration.

1.6 Hydrogel Matrices for Cell Encapsulation

In the realm of cell therapies, the encapsulation of cells within hydrogel scaffolds has emerged as a common strategy to enhance therapeutic efficacy. Encapsulating cells provides structural support, directs cellular growth, and reduces the risk of **anoikis**; cell death due to detachment from the ECM [116,117]. Additionally, hydrogel scaffolds act as an immunoprotective barrier, shielding cells from inflammatory responses [118–120]. Hydrogels are widely used as scaffolding materials due to their porous structure, which allows for the diffusion of oxygen and nutrients into the scaffold while facilitating waste removal and controlled release of therapeutic molecules [118,119]. Many hydrogels are derived from naturally sourced materials, such as polysaccharides, which have biocompatible, biodegradable, and elastic qualities that closely mimic various tissues, making them suitable substitutes for the ECM [118,119,121]. However, a major limitation of hydrogel scaffolds is inefficient nutrient diffusion. In thicker hydrogels, oxygen forms a gradient, limiting its penetration to the innermost cells, which restricts the scaffold's functional volume to just 5–10% [118,122]. Another limitation is the invasiveness of injecting a bulk hydrogel in tissues, which often requires a smaller specific surface area and may lead to non-uniform polydispersibility.

Many studies have explored cell-based therapies for various applications such as bone defect repair, tendon regeneration, vascular tissue engineering, wound healing, degenerative eye disease and ischemic heart disease. However, major challenges persist. Many cell-based therapies are directly injected into the tissue owing to ease of handling and low invasiveness, but suffer from poor transplantation efficiency, as injected cells are exposed to high mechanical stress, hypoxic microenvironments with limited nutrient supply, and shear forces during injection, reducing their viability [123]. To address these challenges, encapsulating individual cells within micron-scale hydrogel spheres increases the scaffold's surface area, bringing each cell closer to the scaffold's surface. This approach improves cell density, enhances nutrient diffusion, and provides mechanical protection during delivery [118,122,124].

Furthermore, cells tend to disperse and “leak” quickly from the injection site, further limiting their therapeutic impact [123]. Also, the host tissue may not provide the necessary biochemical and physical cues for transplanted cells to proliferate and differentiate effectively [125].

Microfluidic hydrogel microspheres offer a promising solution by acting as cell carriers that provide mechanical and biomechanical support during and after injection, improving cell survival and retention [126,127]. Over the past 20 years, significant advancements have been made in microfluidic techniques and the design of hydrogel microspheres for various applications. Progress has mainly focused on developing fabrication devices, refining production methods, enhancing cell and drug encapsulation strategies, optimizing delivery approaches, and expanding biomedical applications [123].

Following injection, hydrogel microsphere carriers can offer stable mechanical and physical support to both the encapsulated cells and the surrounding tissue [126]. This is particularly relevant for Keratoconus patients, where corneal thinning and curvature loss require mechanical reinforcement while cells take time to regenerate the stromal tissue. Also, like previously mentioned, hydrogel biomaterials can be engineered to incorporate bioactive molecules that guide cell behavior and enhance material performance, promoting the regeneration of the target tissues. One notable example in the literature is the use of hydrogel scaffolds combined with mesenchymal stem cells (MSCs) for treating infarcted heart tissue. Encapsulated Mesenchymal Stem Cells (MSCs) transplanted at the site of myocardial infarction (MI) have been shown to remain viable for weeks after implantation, whereas non-encapsulated cells injected as a suspension are nearly undetectable after a short period [128,129]. This prolonged cellular residence often correlates with improved heart function in animal models, with clearly visible reductions in infarct size [128,130].

A key limitation that still lies in the field is the limited selection of biomaterials available for hydrogel microsphere formation. Only a few types of natural macromolecules and synthetic polymers are currently used for microfluidic hydrogel microsphere formation in research applications. Future advancements will require the development of novel biomaterials with superior raw material biocompatibility, stability, and functional tunability to expand the clinical use of cell-encapsulating microspheres in regenerative medicine and targeted therapeutic delivery.

Our synthetic collagen like peptide represents an excellent candidate for expanding the use of microfluidics systems in microsphere formation and cell encapsulation[93]. The success of our formulation lies in the unique hybrid peptide-copolymer system, which enables tunable physical

properties tailored to specific tissues or clinical applications simply by adjusting the chemical sequence or even reaction stoichiometry. With only two components to prepare the hydrogel, our synthetic collagen like peptide and an 8-arm PEG-maleimide crosslinker dissolved in buffer, this hydrogel system offers rapid in situ gelation, minimal chemical complexity (so high likelihood to be used as a delivery mechanism), tunable mechanical properties (depending on application, hydrogel strength, adhesivity, and a well-defined chemical composition), post-synthesis modifications, making it a versatile candidate for cell delivery microsphere systems. Given these attributes, our hydrogel-based microsphere platform holds great promise for use in microfluidics systems and cell therapy applications in Keratoconus treatment, as well as broader applications in tissue regeneration **(Figure 2)**.

1.7 Bridging the Gap: Thesis Objective to Address the Unmet Need

This study addresses a critical unmet need in soft tissue repair by tackling key challenges in cell-based therapies, injectable biomaterials, and microfluidic systems for cell delivery and encapsulation. Building upon our previous established work on synthetic collagen like peptide (CLP) injectable hydrogel utilizing click chemistry between thiol and maleimide groups, we hypothesize that a novel approach integrating our pre-established peptide technology system with micro-sized cell-encapsulating spheres can be used for targeted corneal delivery in Keratoconus applications. We will optimize the click chemistry technology to fit the formation of quick gelling microspheres encapsulating cells, evaluate the success of this encapsulation with a series of Live/Dead assays using different cell lines, characterize the microspheres and compare them to pre-established agarose microspheres as control, and finally perform *ex vivo* testing of the cell-encapsulating microspheres by injecting them in a synthetic cornea and observe them over time.

By overcoming the limitations of conventional cell injections and bulk hydrogel scaffolds, our approach seeks to develop a hybrid system that not only enhances cell retention and viability but also provides an ECM-mimicking scaffold to support thinning corneas. With this proposed innovative delivery and encapsulation strategy, we hope to put forward another way in which biomaterials can improve the delivery and performance of pharmaceutical compounds or cell therapies for regenerative medicine applications.

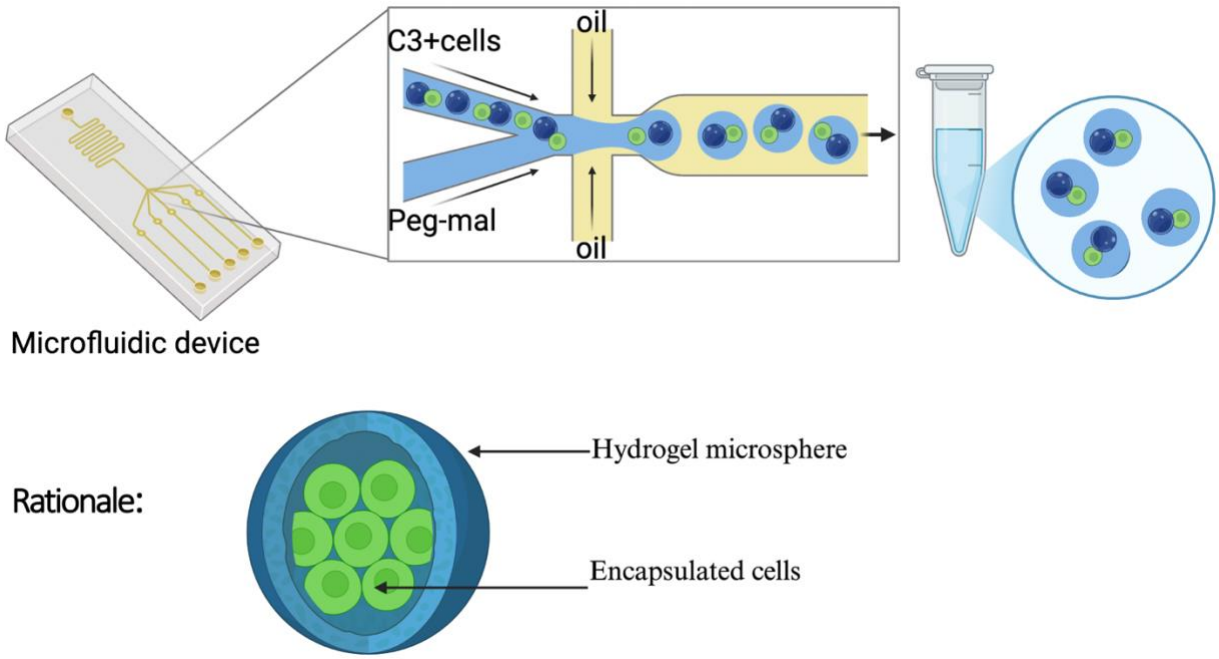

Figure 2. Schematic representation of a microfluidics system designed to generate collagen-like peptide-based microspheres for cell encapsulation. The process involves combining CLP+ cells and PEG-Mal within a microfluidic device, followed by emulsification in oil to form stable microspheres. These microspheres feature an inner core containing cells.

Project aims

Aim 1: Develop a cornea specific injectable peptide-based biomaterial with optimized mechanical properties and the ability to reshape corneal curvature.

Aim 2: Optimize the material formulation with a biologically compatible sequence that integrates with an established microfluidic system to generate microspheres capable of encapsulating and delivering cells.

Aim 3: Characterize the microspheres' mechanical and chemical properties.

Methods

2.1 Peptide Synthesis

The synthesis of our synthetic collagen-like peptide sequences was done following a pre-established method [93]. The peptide is gone through a process of synthesis using the Fmoc solid phase peptide synthesis in a Liberty Blue automated system, then undergoes a lyophilization process before being placed in powder form in glass vials in the desiccator to control humidity and dryness. Fmoc-protected amino acids and low-loading Wang resin were used. Briefly, the resin was swelled in DMF, and Fmoc deprotection was carried out with 20% piperidine at 90℃. Standard coupling cycles using DIC/Oxyma Pure were conducted at 90℃. Peptides were cleaved from the resin, deprotected, and precipitated in diethyl ether. The crude peptides were dried under vacuum, purified by preparative RP-HPLC, and confirmed for purity and identity via analytical LC-UV/MS. A purity of >95% was determined through HPLC peak analysis.

2.1.1 Collagen-Like Peptide Optimization

Our team has previously followed a Michael addition kinetic principle to select sulfhydryl groups which rapidly react well with PEG-maleimide and selectively form a stable hydrogel. The amino acid that contains a reactive sulfhydryl group is cysteine which is why it was included in each strand of the peptide design (**Figure 1**). Then, we used a high throughput low volume approach to test different peptide formulations. First, we monitored the stability of Peg-maleimide in carbonate buffers which showed stability at low temperatures and slightly basic pH 7.4 and stability at low temperatures (<4.0ºC) was good for 90 mins. In preparing our materials, we prepared different ratios of CLP peptide: PEG (1.0, 3.0 and 4.0 (cornea)) and tested them for their ability to form a hydrogel in a clinically relevant time frame (between 15 to 120 seconds). Next, our team tested transmittance (>85%), refractive index (<1.380), denaturation temperature (>42 degrees), water content (>85%), and the stability in type 1 collagenase solution which was a degradation rate for a 1.0% hydrogel in solution. Further, since our goal is to develop a clinically translatable material that can encapsulate cells, we designed the physical properties of the material prior to hydrogel formation to make them deliverable via a ≈400 μm cannula (G27 needle) or in the form of a topical/superficial application. The hydrogels were prepared from three components: peptide, 8-arm PEG-maleimide, and a buffer solvent (different buffers were used in the optimization process

including PBS, Ammonium Bicarbonate, Tris-HCl, MES, Hank's Buffer and DMEM cell media). Reagents were freshly dissolved in buffer before use and kept on ice until application. For optimization testing, peptide concentrations ranged from 3.5 mM to 16 mM while PEG concentrations tests ranged between 2 to 5 mM.

To find the best peptide candidates with strong mechanical properties that can preserve their microsphere structure under the microfluidic system and encapsulate cells at the same time, different characteristics of multiple peptide candidates (differing based on sequence and motifs) were tested. The optimized formulation was chosen based on its ability to create hydrogel microspheres in the microfluidic system, withstand centrifugation and preservation for multiple weeks, and be biocompatible with encapsulated cells maintaining healthy morphology.

The optimal sequence for our collagen like peptide was determined by testing various concentrations, buffers, and microfluidic systems. The chosen candidate showed ability to form spherical hydrogels (microspheres) and showed proper cell encapsulation efficiency and viability of those encapsulated cells.

2.1.2 Hydrogel Formation

Two different hydrogels were formed in this study: our synthetic collagen-like peptide and the control hydrogel agarose. The Ultra-Low Gelling Temperature agarose purchased from Sigma is initially in powder form and needs to be dissolved into a gel before use [131]. Higher concentrations of agarose, around 3% and above, gel easily at the working temperature, but have higher viscosities that can negatively affect the formation of a dispersed phase. On the other hand, lower concentrations around 1% tend to be too weak to properly encapsulate cells upon gelling due to the thin networks that form [132]. Therefore, for this project, agarose concentrations between 1.5% and 2% are used for cell encapsulations. To prepare the agarose, a higher concentration of 2.7% is initially made to allow for mixing with a cell suspension to reach the desired concentration. A larger stock of 3 mL is prepared and stored at 4ºC until needed. The agarose powder is added to sterile PBS in a falcon tube, which is then placed in a beaker of water in the microwave. Next, heating and vortexing steps are done alternatively until the agarose reaches near boiling and is

fully dissolved, typically within 1 to 1.5 minutes of heating in 10 second increments. The stock will melt into a usable liquid state upon heating to above 65ºC but will gel when stored at 4ºC.
For the collagen-like peptide hydrogel, the preparation involves mixing 2.5 mM of the collagen-like peptide with a dissolving buffer (PBS) and combining it with 5 mM of PEG-Mal in the same buffer. These two solutions are mixed within the microfluidic system to produce immediately gelled microspheres. Therefore, the solutions must be kept separate until the microfluidic run is ready.

2.2 Cell Culture

GFP tagged Human Fibroblast cells (GFP+HFBCs) were cultured using DMEM media supplemented with 10% FBS and 1% Penicillin/Streptomycin to provide necessary nutrients and prevent bacterial contamination. From this point forwards unless stated otherwise, "media" refers to this mixture. GFP+HFBCs stored in cryovials in liquid nitrogen were thawed with media. This step dilutes the DMSO used for freezing, which could be harmful to thawed cells. The cell suspension was centrifuged at 1100 RPM for 5 minutes, and the supernatant was aspirated. The cell pellet was then resuspended in media and transferred to a T75 cell culture flask and incubated at 37 ºC, with 5% CO2 to ensure optimal cell growth conditions.

Media was changed every 2 to 3 days by aspirating half or all the existing media and replacing it with an equal volume of fresh media. When cells reached 80% confluency, they were passaged to prevent overcrowding. Cells were detached using 0.25% Trypsin EDTA, counted and transferred to new flasks or used in experiments. Briefly, passaging started with aspirating the media, and washing the cells with PBS to remove any residual media or dead cells. Trypsin is then added to coat the cells, media is added to neutralize it, which is then centrifuged at 1200 RPM for 5 minutes. Cells are resuspended in media for further culturing. (**Figure 3)**.

For time-lapse or time point experiments, well plates were prepared with 2 mL of media, and a cell suspension concentration of 8.5 million/mL. Any remaining cells were bleached and properly disposed of according to safety protocols.

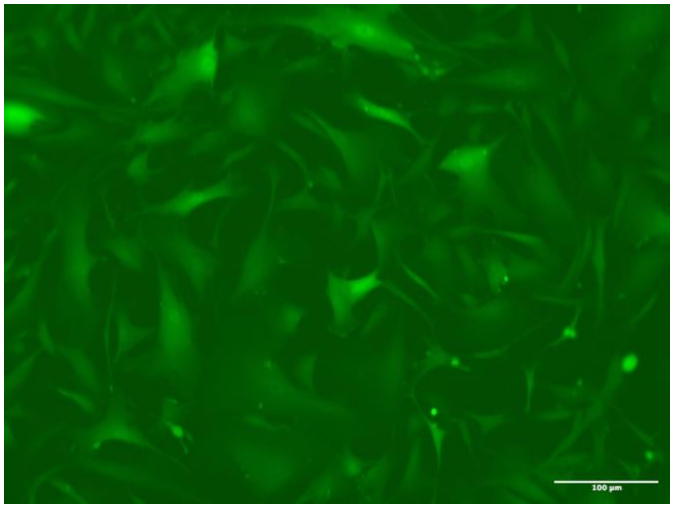

Figure 3. Adherent layer of GFP+ Human Fibroblast cells.

2.3 Microfluidic System Fabrication

Various designs of the microfluidic systems were developed to identify the most optimal for the study's objectives and biomaterial being tested. The typical designs used for gelatin and agarose were not suitable for our two solutions-based on-the-spot gelling peptides. However, the fabrication method followed the protocols published by the Godin lab [133]. Briefly, the microfluidic devices were created using soft photolithography processes adapted from previous methods [134,135]. Photolithography involves creating molds with SU-8 photoresist on 100 mm silicon wafers. PDMS is then poured onto these molds and cured. After curing, the individual channels are cut from the mold and bonded to glass slides.

The device we ultimately selected for the remainder of the experiments, after various rounds of optimizations, included:

- An inlet channel of 50 µm, leading into a 70 µm oil channel, 35 µm nozzle with a 50 µm inlet channel pinching that leads into a 280 µm spacer channel
- The channel widens to a 360 µm opening
- The other end of the device includes a serpentine with 6 loops (50 µm) to give the biomaterials time to gel, then an outlet with a looser spacing than the top inlet

2.3.1 Encapsulation Device Preparation

Outside of the channel, there are external components that build around the glass slide to control the temperature and fluid flows on chip, and to visualize what is happening in the channel. Samples and oil were introduced into the device using PEEK tubing (1/32'' outer diameter, 0.007'' inner diameter) with pressure-driven flow regulated by manual pressure regulators and solenoid valves. Flow rates were controlled through a shared air source to ensure stability, with continuous and dispersed phase pressures ranging from 34 kPa to 172 kPa and 34 kPa to 152 kPa, respectively. Custom LabVIEW software enabled precise control of flow activation. Encapsulation was achieved through a flow-focusing mechanism, where oil pressure was applied through two PEEK inlet tubes simultaneously. The generated microspheres were collected in an outlet vial containing DMEM in an ice bath.

The device was mounted on a VWR Inverted Microscope equipped with a Point Grey 60 FPS USB camera and SpinView software for real-time monitoring **(Figure 4)**. The microscope stage allowed XY mobility, and various objective lenses provided different magnifications. A contrast filter was used to enhance imaging, particularly for observing agarose gelling.

2.3.2 Encapsulation Process: Microsphere Formation

Before encapsulation, a sterile water-in-oil emulsion was prepared to check for leaks or device flaws and to assess device-to-device variability. Sterile mineral oil (purchased from Sigma-Aldrich) was used as the continuous phase, supplemented with 2% Sorbitan Monooleate (Span 80) surfactant to facilitate monodisperse droplet formation while maintaining low cytotoxicity. The emulsion was prepared by micro pipetting Span 80 into the mineral oil, followed by vortex mixing for uniform dispersion with PEG-Maleimide (To create a PEG-Mal emulsion: 950 uL of 2% Span 80 in oil and 50 uL of 5 mM PEG-Mal). The reason we added Span80 into PEG-Maleimide and not the collagen like peptide (CLP) is due to PEG-Mal having a higher viscosity in the device than the CLP. Additionally, PEG-Mal has a different higher viscosity than our CLP. The latter is introduced into another inlet mixed with cells. As the flow of these two inlets meet, the microsphere encapsulating cells are created.

After stabilizing the water-in-oil emulsion and preparing the sample, the dispersed phase inlet is replaced. This involves stopping the flow, detaching the sample vial, inserting the PEEK tubing into the glass insert containing the two samples (2.5 mM of collagen like peptide with cells in media; and PEG-Mal dissolved in DMEM media and mixed with Span 80 and mineral oil emulsion), and resuming flow. Cells are in the peptide solution at around 20 mil/mL concentrations. Peptide and oils are introduced through 0.01" ID (Inlet diameter), and 0.0007" ID PEEK tubings respectively. The peptide is emulsified using a 50 μm flow focusing nozzle, while PEG is introduced as a coflow sandwiching the peptide-in-oil emulsion to ideally mix small PEG droplets into the larger peptide droplets to gel them. Fluids are introduced to the device using air pressure from central air, passed through regulators.

To enhance throughput, both pressures are increased while adjusting the ratio to compensate for changes in hydrogel viscosity and surface tension. The peptide is 18 PSI, while the two oil inlets are at 12 PSI, adjusted slightly to make proper flow. To fine-tune the microsphere size, the sample pressure is modified. Microsphere sizes are measured using SpinView snapshots and analyzed with ImageJ, using the channel width as a reference. When the desired size is reached, the outlet tube is switched from waste collection to a 500 μL DMEM-filled microcentrifuge tube kept in an ice bath to preserve cell viability. The entire encapsulation process is continuously monitored to ensure consistency, with pressure adjustments done as needed throughout the encapsulation.

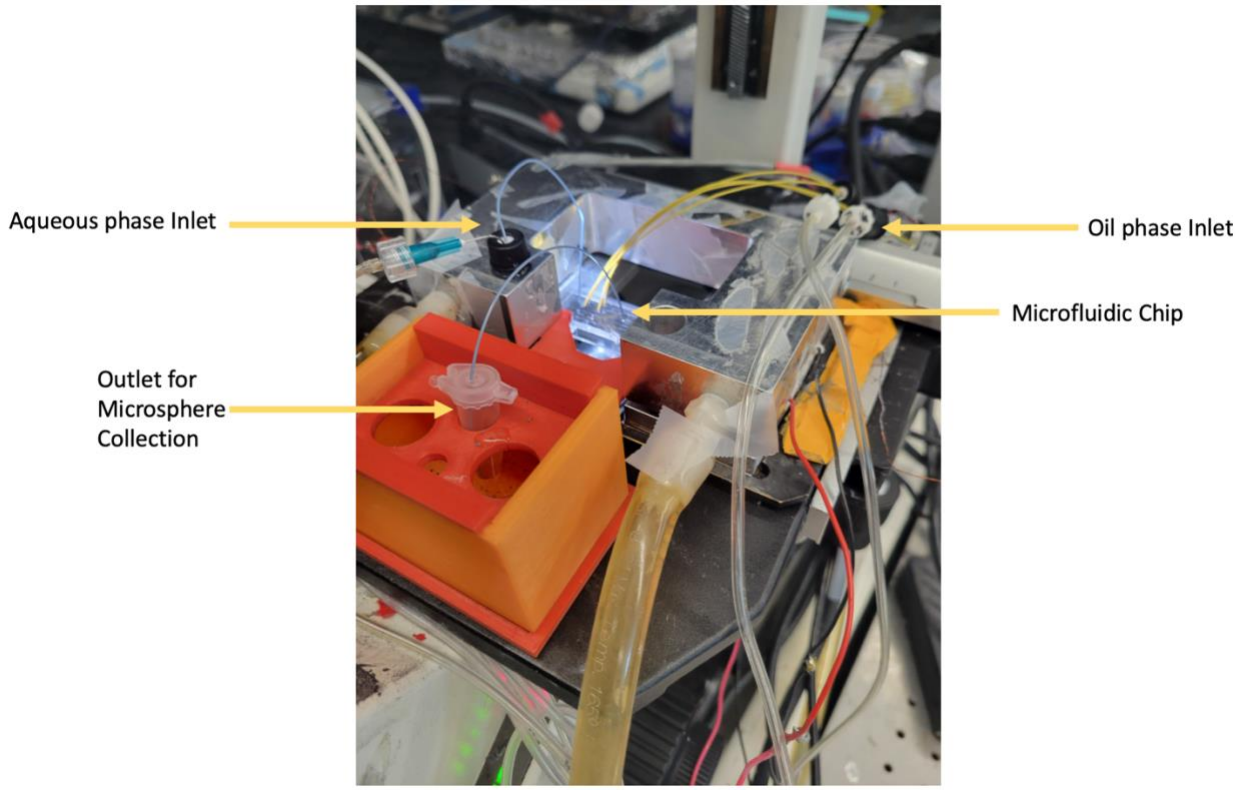

Figure 4. Picture of microfluidics system set-up on inverted microscope.

2.3.3 Post-Encapsulation Purification

Once the encapsulation process is complete, the oil phase needs to be removed from the sample to avoid its interference with cells or the biomaterial itself. This is done by using a microcentrifuge for 2 or 3 rounds. Centrifuging at 0.3xG for 3 minutes is enough to move the microspheres from the oil phase to the aqueous phase and pellet the microspheres, without reducing cell viability. After centrifuging, a micropipette is used to remove the oil phase and the process is repeated. After the second time, the pellet needs to be broken up in the aqueous phase and moved to a new vial as the initial vial will still be coated with remaining of the oil phase. The sample is kept on ice until ready to plate with media for further testing and incubation.

2.3 Cell and Microsphere Quantification: Fluorescence

Brightfield microscopy was useful for visualizing the presence of cells in microspheres, and phase contrast microscopy highlighted differences in diffraction. However, neither method could easily show the viability of the encapsulated cells in microspheres. Therefore, two different fluorescent dyes were used that emit at different wavelengths and are associated with different cellular

activities to determine cell viability. A live/dead assay was performed using Calcein, a green dye converted into a fluorescent material by enzymes in living cells, and Ethidium Homodimer-1, a dye excluded by living cell membranes but fluoresces when bound to DNA, to identify live and dead cells.

Using image processing, the images from the live and dead fluorescing dyes were combined with the brightfield image to create a composite image where live cells are clearly marked in green, and dead cells are marked in red [136]. To stain the cells, the two dyes were mixed at a concentration of 1 μM and incubated for 30 minutes before imaging.

The occupancy of microspheres was calculated as the number of microspheres containing cells divided by the total number of microspheres, and cell viability was calculated as the number of living cells divided by the total number of cells. These values were determined by counting the microspheres and cells observed in fluorescence microscopy images. Counting was performed manually using ImageJ software, noting the number of microspheres, the number of cells within microspheres, and the number of living and dead cells.

2.3.1 Timepoint

To determine the statistics of how cell viability inside the hydrogel and agarose microspheres occurs over longer periods of time, a series of fluorescence/brightfield images or live dead assays were taken over the course of 72 hours. This length of time was chosen as after this, the media begins to run low on nutrients and replacing it would cause losses and disruption to the loose microspheres. Microspheres were distributed into well plates containing DMEM culture media, with approximately 10,000-20,000 microspheres per well. At designated time points (2 hrs, 24 hrs, 48 hrs, and 72 hrs), seven images were captured per well to assess occupancy and viability.

Microsphere occupancy was determined by counting microsphere containing cells. It was calculated as the proportion of occupied microspheres relative to the total number of microspheres.

Cell Viability was assessed by calculating the proportion of living cells inside the microspheres relative to the total number of cells.

2.3.2 Hemocytometer for initial microsphere counting and throughput calculation

Microsphere quantification was performed using a hemocytometer. The number of microspheres in four large corner squares was counted and averaged. This value was then multiplied by the total sample volume (in mL) and by 10,000 to account for the hemocytometer's volume, providing the total microsphere count in the sample.

To determine production throughput, the start and end times of sample collection were recorded, and the total number of microspheres produced was measured. The average production rate was calculated as the number of microspheres generated per second over the entire run. However, this method required a large sample size for accuracy, making real-time throughput "snapshots" impractical.

2.3.3 ImageJ for Measuring Microsphere Sizes

The basic pixel-based measuring feature in ImageJ allows users to set each pixel to be worth an amount of real distance to measure the size of features from collected images. This method was used to measure the size of microspheres in real time as they were being made in the microchannel. The known width of the microchannel, visible in all images where microspheres were being measured, serves as a reference scale to calculate the length corresponding to each pixel. Lines were then drawn to bisect the microspheres, taking measurements of each (**Figure 5**). Microspheres can vary in size due to several factors, including intentional adjustments in pressure settings, size drift caused by changing conditions within the channel over time, or polydispersity, where cocoons produced within a specific timeframe exhibit variations around an average size.

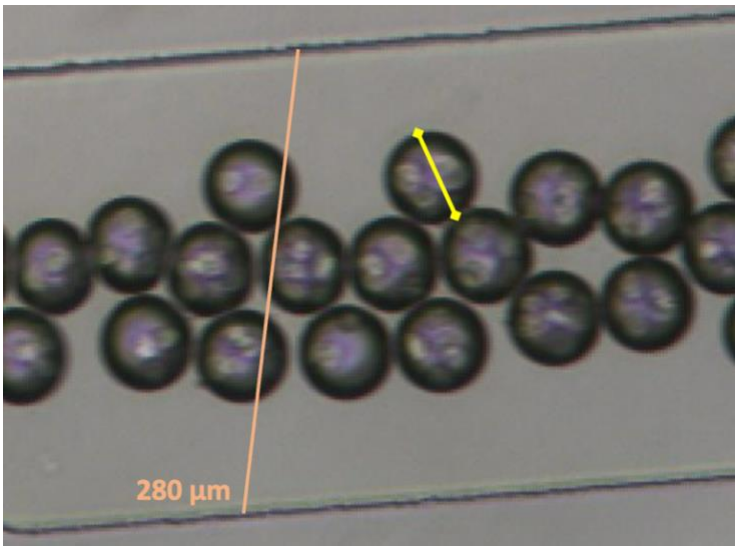

Figure 5. Image J method of measuring microsphere size. First a line is made over the position of the added orange line, which sets the # (number) of pixels in that line to be equivalent to 280 µm. Next lines such as the yellow line are made that bisect each microsphere to provide the measured size.

2.4 Microsphere Characterization Tests

Different tests were conducted to characterize different properties of the hydrogel and agarose microspheres. Some were prepared in bulk hydrogel to establish more accurate results.

2.4.1 Material Viscosity/ Shear Stress Rheological Test

The viscosity measurement was carried out using a Kinexus Lab rheometer with a parallel plate geometry (20 mm diameter), and the data were analyzed with the rSpace software. The samples were spread on a 20 mm parallel plate and sealed with a silicone cap to prevent solvent evaporation. Measurements were taken at different shear rates (from 0.01 to 100 s-1) at 37°C.

2.4.2 Collagenase Degradation

Hydrogel stability was evaluated by enzymatic degradation after swelling using collagenase from *clostridium. Histolyticum* (sigma-Aldrich, USA). Samples were incubated in a solution containing 5U/mL collagenase in 0.1 M Tris Buffer (pH 7.4) supplemented with 5 mM $CaCl_2$ at 37 °C. Samples were retrieved at predetermined time points, rinsed with deionized water to halt

enzymatic activity, and weighed. The percentage of residual mass was calculated using the following equations: Residual mass (%) = W_t/W_0 x 100 **(Eq. 2.1)**.

2.4.3 Swelling behavior of hydrogels

Hydrogel swelling was evaluated by incubating 10 – 5 mg of hydrogel samples in 1x phosphate buffered saline (PBS, pH 7.4) at 37 °C. Samples were allowed to equilibrate for 48 hours, and swelling was monitored at defined time intervals (e.g. 1,2,3,4,5,6,24,48 hours). At each time point, the hydrogels were gently removed, and excess surface water was removed with a Kim wipe and weighted. The swelling ratio was calculated using the following equation: Swelling (%) = $(W_t-W_0)/W_0$ x 100 **(Eq. 2.2)**, where W_t is the swollen weight at time t, and W_0 is the initial weight of the hydrogel.

2.4.4 Thermal Characterization/DSC (Denaturation Temperature)

The thermal properties of the hydrogels were analyzed using differential scanning calorimetry (DSC-Q200, TA instruments, USA) samples (8-10 mg) were hermetically sealed in aluminium pans and equilibrated at 10 °C. The temperature was then increased at a rate of 10 °C/min to 100 °C, and total heat flow was recorded. Indium was used as the calibration standard for temperature and enthalpy. The glass transition temperature (Tg) was determined from the inflection point of the heat flow curve.

2.4.5 CD spectroscopy analysis

2.4.6 Circular Dichroism (CD) Spectroscopy to assess Folding and Melting Temperature

Circular dichroism (CD) spectra were recorded using JASCO J-810 spectropolarimeter equipped with a Peltier temperature controller (MPTC-490S) measurements were performed at 20 °C using a 0.5 mm path length quartz cuvette and a bandwidth of 1.0 nm, over the far-UV range of 190-260 nm. Samples were initially prepared at concentrations of 200 µM in 1 mM phosphate buffer (pH 7.4), followed by serial dilutions to 100, 50, 25, 12.5 and 6.25 µM to assess secondary structure across different concentrations. For each condition, spectra were recorded as an average of 10 scans, with solvent background subtraction applied. The mean residual ellipticity (RPM) and melting temperature (Tm) were extracted from the spectra to evaluate folding behaviour and thermal stability.

Melting curves were obtained by monitoring the ellipticity at 225 nm using circular dichroism (CD) spectroscopy as temperature increased from 20°C to 75°C. A decrease in signal indicated unfolding of the triple-helical structure. The melting temperature (Tm) was defined as the midpoint of this transition. This analysis was used to compare the thermal stability of C3 and C30 peptides and identify the most stable candidate above 37°C.

2.4.7 SEM

Pore size was measured using a standard cryo-SEM protocol previously established [137]. Briefly, microsphere hydrogel samples were dropped on an aluminum SEM sample stub, and flash-frozen with liquid nitrogen. Then it was transferred to a Peltier cold stage of the cryogenic SEM (Tescan VegaII XMU (20 kV) with temperature setting below -40 °C. The hydrogen was imaged using environmental SEM (Low Vacuum SEM) method with the vacuum/pressure above 40Pa using 20KV acceleration voltage. SEM images of hydrogels were captured at different magnifications. This method of rapid freezing and measurement helps to preserve the material's structure and pore size before processing [138]. Hydrogel pore diameter was calculated from the average pore area observed in different regions of the gel using Fiji software.

2.4.8 Microspheres Preservation

The preservation capability of the microspheres was assessed by storing them either in an incubator (if cells were encapsulated) or in a 4°C refrigerator (if no cells were encapsulated) and recording the duration of viability. Microspheres containing cells remained viable for up to 3 weeks, after which they were discarded. Microspheres without cells retained their shape and viability in the refrigerator for approximately 4-5 weeks before samples were used up in other experiments and were no longer available for further storage observation.

2.4.9 Infrared Spectroscopy

Fourier-transform infrared (FTIR) spectra were recorded using a Nicolet iS5 FTIR with an Attenuated Total Reflectance (ATR) iD7 accessory and with a diamond crystal. All spectra were taken at 4 cm-1 of resolution, and 64 scans in the 4000-500 cm-1 range at room temperature. Before measurements, the prepared peptides and hydrogels were freeze-dried.

2.5 Statistical Analysis

Data was presented as a mean ± SD. Analysis was performed using Microsoft Excel and GraphPad Prism, where *p* values greater than 0.05 were deemed to be not significant. Differences between two groups were evaluated using a two-tailed unpaired Student's t-test.

Results

The purpose of this research project is to investigate the feasibility and methodology of whether our lab-developed collagen-like peptide (CLP) hydrogel could be adapted for microfluidic encapsulation of cells into microspheres, using a Michael addition reaction between a thiol-containing CLP and an 8-arm PEG-maleimide. The objective was to assess the impact of this encapsulation method on cellular viability and proliferation, based on the hypothesis that an immunoprotective permeable hydrogel barrier could provide an open yet supportive environment for cells, potentially leading to improved cell survival compared to conventional suspension-based delivery. Unlike direct cell injections, which often suffer from poor retention, early clearance, or suboptimal cell survival in vivo, encapsulation within supportive scaffolds has been shown to significantly improve therapeutic outcomes. Our approach aimed to compare this method with established standards such as for agarose-based microspheres, frequently used in similar applications. Should this hypothesis hold up, these synthetic collagen microspheres could offer a significant advancement in cell-based regenerative therapies, providing an alternative to conventional approaches that rely on solid bulk hydrogels or the direct injection of cells in suspension, which lack a structural support surrounding system.

To test this, the study consisted of optimizing the previously developed CLP hydrogel—originally used for bulk injection into corneal, dermal, and cardiac tissues—into a formulation compatible with microfluidics processes. Our previously developed synthetic CLP had shown promise in earlier studies for tissue repair applications due to its tunable mechanical properties and rapid gelation. However, integrating it into a microfluidic system posed significant challenges, as existing microfluidic devices are typically designed for materials like agarose and gelatin, which crosslink under very different conditions. Thus, this study involves two main challenges: (1) optimizing the CLP hydrogel formulation for microfluidic droplet generation, and (2) developing a microfluidic chip design compatible with the rapid, on-the-spot gelation chemistry of our hydrogel system.

First, two hydrogel biomaterials, agarose and CLP C30, were investigated for their ability to generate stable microspheres in a flow-focusing microfluidic platform. Experimental parameters such as CLP concentration, surfactant concentration, and hydrophilic-lipophilic balance (HLB)

were systematically varied to identify optimal conditions for creating stable emulsions for an improved microsphere formation.

Subsequent experiments assessed this optimized microsphere system by encapsulating cells within the formed microspheres. Characterization experiments were done to assess microsphere morphology, mechanical properties, and encapsulation efficiency. Live/dead staining assays were performed to monitor cell viability and proliferation in time point studies. Comparative studies included both agarose microspheres and two controls, C3 CLP, and native collagen, to evaluate the bio functionality and tunability of the optimized C30 formulation.

Microfluidic Device

To begin generating the microspheres, the first step was designing a microfluidic device that could accommodate the unique crosslinking chemistry of our CLP biomaterials. Unlike agarose or gelatin, which gel thermally or via ionic interactions, the CLP/PEG-Mal system undergoes rapid Michael-type addition, forming a hydrogel almost instantly upon mixing. This meant pre-mixing the two components before entering the chip was not an option—doing so would result in early gelation before the fluids even reached the droplet-generating junction, rendering the system unusable. This necessitated the design and testing of new microfluidic devices capable of mixing the two hydrogel components inside the chip just before the droplet formation.

We hypothesized that a microfluidic system with two head inlets could work for generating fully gelled CLP microspheres. Four microfluidic designs were tested, all with variations in inlet configuration, nozzle size, and channel geometry. **Figure 6A** shows a two-head inlet device with no mixing channel and a 90 µm nozzle. While it allowed for initial flow, gelation occurred too quickly, leading to clogging in the device as represented by the brightfield images. **Figure 6B** introduced a mixing serpentine to the same two-inlet design (80 µm nozzle), which aimed to promote better pre-junction mixing but resulted in even faster clogging due to the extended residing time. **Figure 6C** moved to a three-inlet system with asymmetric channel widths (90 µm nozzle, 400 µm main channel, 60 µm middle, 95 µm side). This setup allowed for some spatial control of the streams but still failed to produce stable microspheres, with gelation and blockage occurring early in the process. Finally, **Figure 6D** modified the previous geometry by incorporating an oil phase with surfactants to help stabilize the PEG-Mal emulsion and limit

premature crosslinking. This version showed the most promise, although clogging was still an issue, it was the only device that produced recognizable, discrete microspheres.

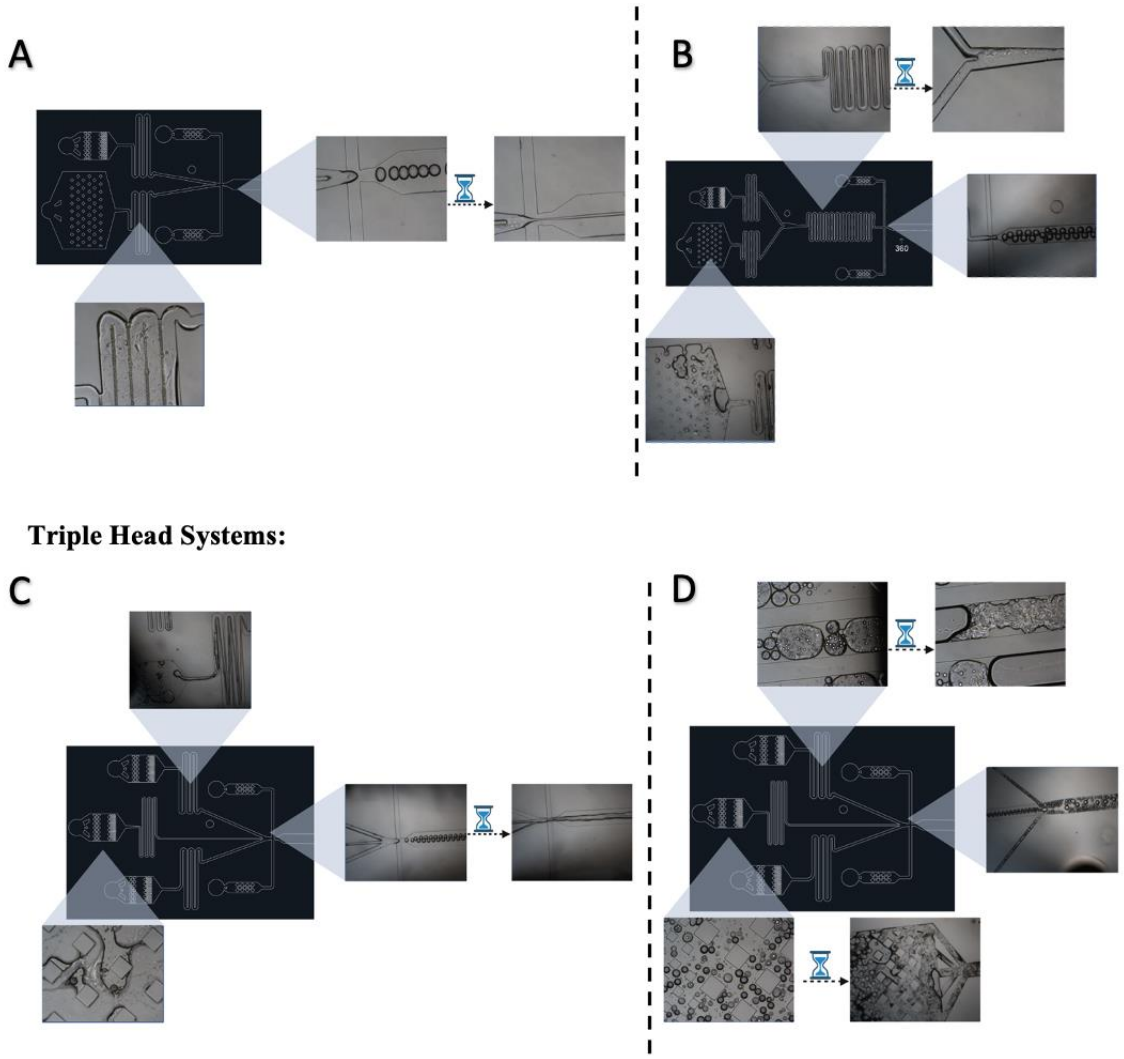

Figure 6. Optimization of microfluidic systems for optimal application of hydrogel technology. A) Device with 2 head inlet and no mixing serpentine with a 90 µm nozzle. Images show gelation and clogging of device. **B)** Device with 2 head inlets with the addition of a mixing serpentine with an 80 µm nozzle. Images show gelation and clogging of device. **C)** Device with 3 head inlets with 90 µm nozzle, 400 µm main channel, 60 µm middle channel and 95 µm side channels. Images show gelation and clogging of device. **D)** Same geometry as C with the addition of a surfactant emulsion. Images show some sphere formation before early gelation and clogging in device.

The previously designed microfluidic systems used in the Godin Lab accommodate gelatin and agarose as materials. The key characteristics of these systems are illustrated in **Figure 7** labeled as "initial design". Briefly, the initial design featured 2 oil inlets and a single inlet for the material (agarose or gelatin were typically used), a 35 μm nozzle flanked by symmetrical channels with widths of 50 μm and 300 μm, merging into a wide outlet of 900 μm. This configuration worked best for agarose and gelatin. However, it did not work for our CLP-C30 peptide which depend on the thiol-maleimide interaction to form stable hydrogels. In contrast, the updated design (**Figure 7. Panel A right**) incorporated additional structural elements for improved flow control. The device now includes: an inlet for the C30-CLP+cells, 2 inlets for the oil, and 2 inlets for the PEG+Span80 emulsion. The inlets and outlet diameters were adjusted to 35 μm, 280 μm and 900 μm respectively. A 70 μm wide emulsion inlet was added to facilitate the controlled entry of the continuous oil phase. A coiled serpentine region was also retained and repositioned to improve gelation and residence time of the generated droplets before expulsion through the outlet which was replaced from 2 in the old device to 1 in the updated device. **Figure 7. Panel B** highlights the key functional modules in each design. The initial configuration consisted of an inlet, nozzle, dual outlets, and a serpentine channel. The updated design introduced a dedicated emulsion inlet (purple), and a streamlined flow path aimed to reduce turbulence and improve droplet uniformity. The gelling serpentine region was refined to maintain microsphere shape and prevent premature aggregation or fusion with other partially gelled microspheres.

A

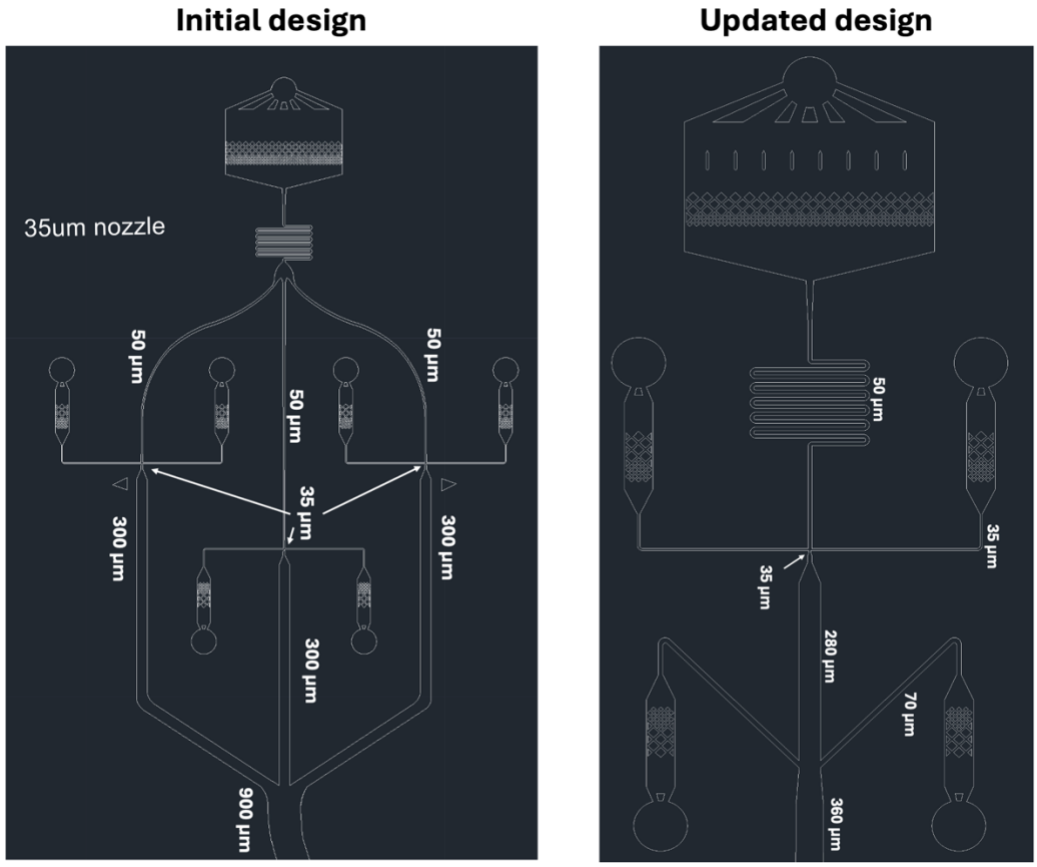
Initial design
Updated design
35um nozzle
50 µm
50 µm
50 µm
35 µm
300 µm
300 µm
300 µm
900 µm
50 µm
35 µm
35 µm
280 µm
70 µm
360 µm

B

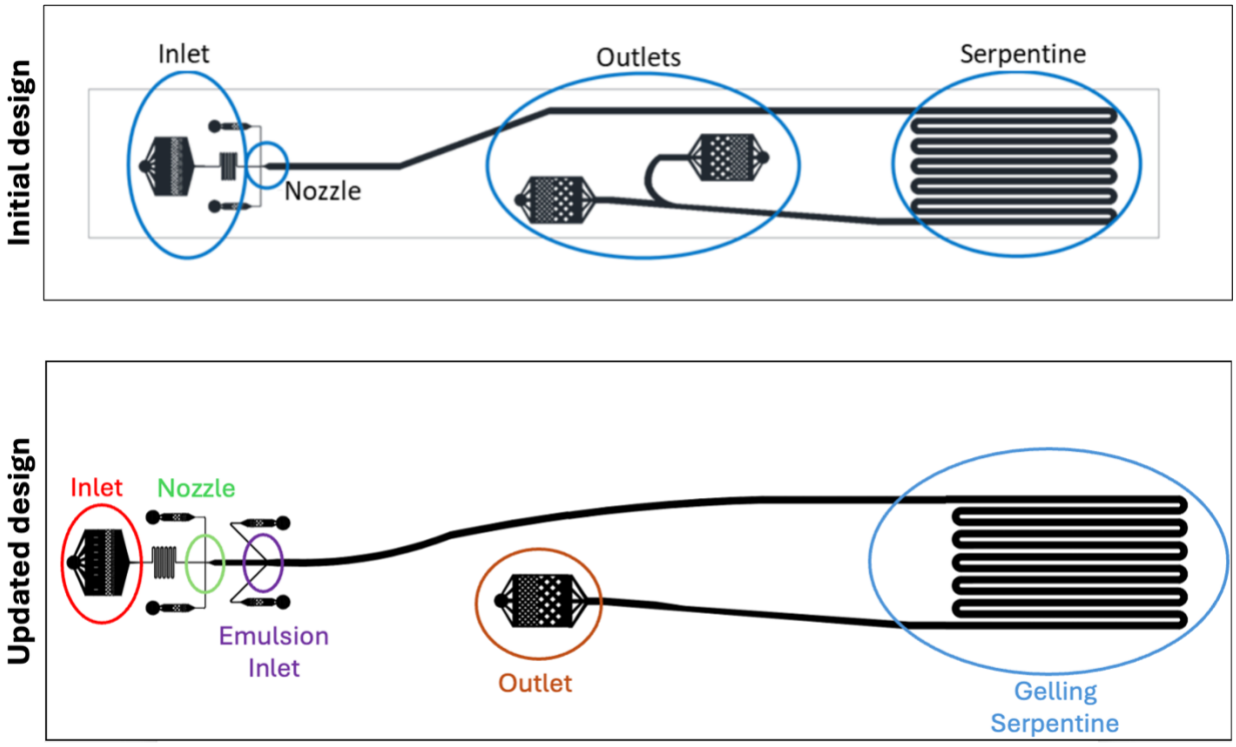
Initial design
Inlet
Outlets
Serpentine
Nozzle
Updated design
Inlet
Nozzle
Emulsion Inlet
Outlet
Gelling Serpentine

Figure 7. Comparison of starting versus current microfluidic system designs for generating cell-encapsulating microspheres. **A)** Device blueprints shows the initial design (left) and the updated design (right) including modifications such as additional structural element and inlet size differences. **B)** Schemes show comparison between the structural elements of each device and their function color-coded elements for clarity (e.g., red for inlets, green for nozzle, blue for gelling region)

One final modification to the updated device included a modified PEG/Oil inlet emulsifier to make finer PEG droplets and contribute to a more stable flow of the PEG-Span80 emulsion mixture **(Figure 8)**. Additionally, the sides of the inlet were carved out to the filters to minimize any unnecessary space for the droplets to get stuck in.

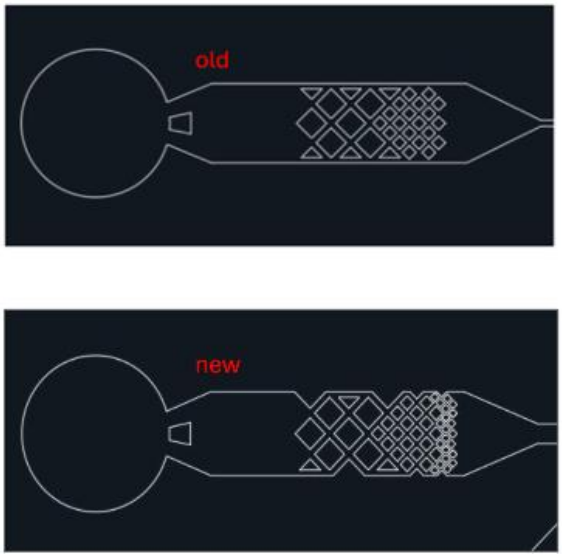

Figure 8. Modified PEG-Span80 Emulsifier Inlet. More filters were included to make finer PEG droplets and unnecessary space from the sides of the inlet were removed.

Hydrogel biomaterials for microsphere formation

The production of cell-encapsulating hydrogel microspheres began by optimizing the collagen-like peptide (CLP) formulation. We have previously developed a library of CLPs with different sequence lengths and motifs owing to different mechanical and chemical properties. The previous applications for injecting thinning corneas and skin incisions with bulk hydrogel showed that CLP C3 (sequence: NH_2-GCG**(POG)$_8$**GCG-OH) was the most optimal in terms of adhesivity, mechanical

strength and gelation time. For this reason, our investigation on extending its application to cell delivery began by testing its behavior in microfluidics. While the use of agarose in these devices is well studied in this research lab in terms of generating a stable monodisperse emulsion, the behavior of other hydrogels is largely unknown [132].

Following the optimization of the microfluidic device, persistent issues with rapid gelation and device clogging hindered microsphere formation. Although the microfluidic runs initially begin smoothly, even minor uncontrolled back pressure led to premature gelation at the inlets, which ultimately clogged the channels and halted device function (**Figure 6. A, B and C**). These observations indicated the need for further optimization of the CLP formulation.

A key challenge identified was the mismatch in viscosity between PEG-Mal and CLP sequence C3, resulting in differential flow rates **(Supplementary Figure S1)**. This imbalance caused irregular mixing at the junction, leading to inconsistent microsphere formation and frequent clogging due to localized gelation. To address this, various concentrations of the surfactant Span 80 were tested to stabilize the PEG-Mal phase and prevent phase separation during emulsification. A stable PEG-oil-surfactant emulsion was essential for consistent droplet generation. Preliminary emulsification trials (**Supplementary Table S1**) revealed that a formulation containing 5 mmol PEG, a 1:10 PEG-to-oil ratio, and 2% Span 80 maintained homogeneity for approximately 10 minutes, sufficient for microfluidic encapsulation. Furthermore, 2% Span 80 was previously validated as the least cytotoxic concentration for use with live cells [139]. Despite these adjustments, significant inconsistencies in microsphere formation persisted. Initial encapsulation showed promising results with stable emulsions and proper microsphere morphology. However, within minutes, the PEG-rich phase began to dominate as the oil phase depleted, destabilizing the emulsion, and leading to droplet coalescence and gelation within the chip (**Supplementary Figure S2**). Although the inlet filter was effective in breaking up the PEG stream into smaller droplets, the absence of a continuous oil phase ultimately resulted in the inflow of pure PEG into the device, exacerbating clogging.

Another recurring issue involved pressure-induced backflow during transfer of the outlet tubing to the collection vial. Even minimal amounts of PEG entering prematurely were sufficient to initiate

gelation and obstruct the microfluidic channels. This problem was mitigated by adjusting the tubing transfer step to occur before PEG entered the system.

Although some microfluidic runs with the C3 formulation yielded discrete, gelled microspheres, the results were not reproducible. Under identical conditions, subsequent trials frequently resulted in early gelation and device failure. These findings suggested that rapid gelation kinetics of the C3-PEG system were incompatible with the droplet generation timeline of the microfluidic platform. Even with varied PEG-Mal concentrations and surfactant levels, C3-based formulations continued to show phase separation and clogging. To overcome these limitations, additional CLP sequences from the peptide library were explored, focusing on variants with slower gelation kinetics to try to mitigate the issue of constant hydrogel clogging the microfluidic device. Different peptide sequences, particularly C35 and C3XF sequences, were tested and either failed to gel entirely or formed large, fused hydrogel masses rather than distinct microspheres **(Table 1)**. The likely contributing factor was that slow gelation allowed the droplets to coalesce and fuse together before crosslinking was complete. Different concentrations of C3 with changing parameters such as the PEG-Mal with the surfactant still resulted in separation of the oil emulsion and lead to device clogging **(Table 1)**. Subsequent screening of another CLP sequence C30, tested at a concentration of 2.5 mM with PEG-Mal concentrations between 2–5 mM, resulted in the formation of individually gelled microspheres, although occasional agglomeration of fused spheres was observed. This formulation demonstrated reduced clogging and improved compatibility with the microfluidic workflow. **Table 2** illustrates the specifications of each sequence tested, including their code, molecular weight, residue number, and mass spectra to confirm peptide identity and purity. These preliminary results supported a transition from C3 to C30 sequence for further optimization and development of monodisperse microspheres suitable for cell encapsulation.

Table 1. Optimization of CLP formulation to generate microspheres by assessing different sequences, concentrations, surfactant concentration, and outcome of microsphere formation. Four different sequences with different concentrations of CLP and PEG-Mal were evaluated.

CLP Sequence Code	[CLP] mmol	[PEG-Mal] mmol	[Span 80] %	Emulsion ratio	Result
C3	3	10	2	20	Emulsion separated Channels clogged
C3	2	5	2	20	Emulsion separated Clamshells formation*
C3	2	5	2	20	Emulsion separated Clamshells formation*
C3	2	5	2	20	Emulsion separated Clamshells formation*
C3	10	3.64	2	20	Channels clogged
C3	10	3.64	2	20	Channels clogged
C30	2.5	2.5	2	5	Clamshells, large full microspheres
C30	2.5	0.75	2	10	Sparse microspheres, poorly gelled
C30	2.5	0.75	2	5	No gelation
C3XF	5	0.75	2	10	No gelation
C3	2.5	0.75	2	10	Large, translucent hydrogel clumps
C3	2.5	0.75	2	5	Large, more defined hydrogel clumps
C3	2.5	0.75	2	20	No gelation
C30	2.5	2.5	2	10	Mix of microspheres and clamshells
C35	2.5	1.25	2	10	Large hydrogel mass
C3	2.5	1.25	2	5	No gelation
C3	5	1.25	2	5	Very low number of microspheres, no gelation

C30	**2.5**	**2.5**	**2**	**5**	**Individual gelled microspheres with some clumps in certain areas**

***Clamshell formation**, as illustrated in the brightfield image below, is the formation of half-moon shaped microspheres as indicated by the red arrows.

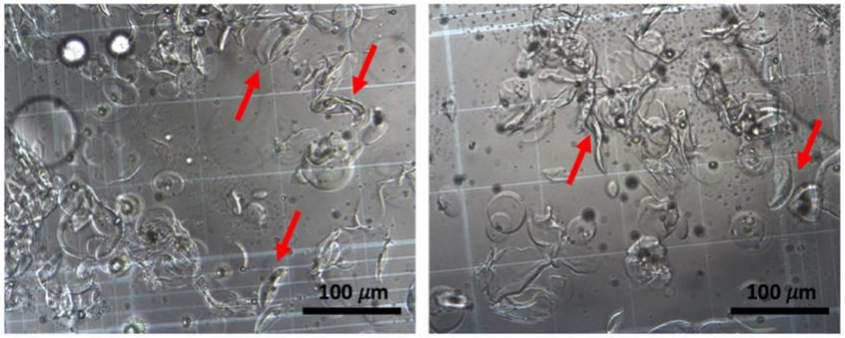

Table 2. List of the tested CLP peptide codes, their sequences, and molecular weights. Mass spectra illustrating detected ions included in the table with representative mass spectrometry data for each peptide presented in the supplementary information (**Supplementary Figures S7 and S8**)

Sample	Sequence	Molecular Weight (g/mol)	Residue Number	M+2H Ion	M+3H Ion
C35	NH_2-GCG**(POG)$_5$**GCG-OH	1789	21	895.5	597.3
C3	NH_2-GCG**(POG)$_8$**GCG-OH	2591	30	1296.4	864.6
C30	NH_2-GCG**(POG)$_{10}$**GCG-OH	3125	36	1563.7	1042.8
C3XF	NH_2-GCG**(POG)$_4$**POV**(POG)$_3$**GCG-OH	2633	30	1317.5	878.7
CLP	NH_2-CG(PKG)$_4$**(POG)$_4$**(DOG)$_4$-OH	3518	38	1759.9	1173.6

Microsphere cell occupancy and viability

To assess microsphere cell occupancy and viability, fluorescence microscopy was used to evaluate encapsulated cell health, distribution, and viability within the hydrogel microspheres. Quantitative analysis included monitoring microsphere counts, localization of cells within the spheres, and the proportion of live versus dead cells over time. Microspheres were observed at multiple timepoints to assess both long-term viability and potential decreases in occupancy, possibly resulting from cell migration out of the hydrogel matrix. In initial experiments using the C3 peptide sequence formulation, some microfluidic runs, although inconsistent, successfully produced microspheres

containing encapsulated cells, which were subsequently analyzed using a Live/Dead viability assay. However, due to the previously discussed issues of inconsistencies, premature gelation, and device clogging, the C3 formulation was ultimately deemed unsuitable for consistent microsphere production.

For the few instances in which C3-based microspheres were successfully generated, viability was tracked over a 72-hour period. As shown in **Figure 9**, cell encapsulation was partially successful at the 2-hour mark. While several microspheres exhibited irregular morphologies, appearing partially formed or collapsed, a subset of well-formed, hollow microspheres was observed, with cells effectively encapsulated within the hydrogel matrix. At this early timepoint, viability was notably high, with a predominance of live cells compared to earlier attempts with the same formulation.

Interestingly, despite the presence of broken or open microspheres in some areas, most encapsulated cells remained contained, and the number of free-floating cells was lower than expected. By the 48-hour mark, rare occurrences of cellular aggregation were noted within the hydrogel structures, yet cell viability across the sample approached nearly 100%. Cells also appeared to adhere to the inner surfaces of some microspheres, indicating compatibility with the internal hydrogel environment. At 72 hours, cell viability remained stable, with no significant decrease compared to the 48-hour observation.

While these results demonstrated a marked improvement in encapsulated cell viability, the inconsistency in microsphere formation using the C3 formulation necessitated a shift in approach. This led to the exploration of alternative peptide sequences, ultimately identifying the C30 formulation as the most reliable for generating monodisperse microspheres with high encapsulation efficiency and minimal clogging, forming the basis for subsequent experiments.

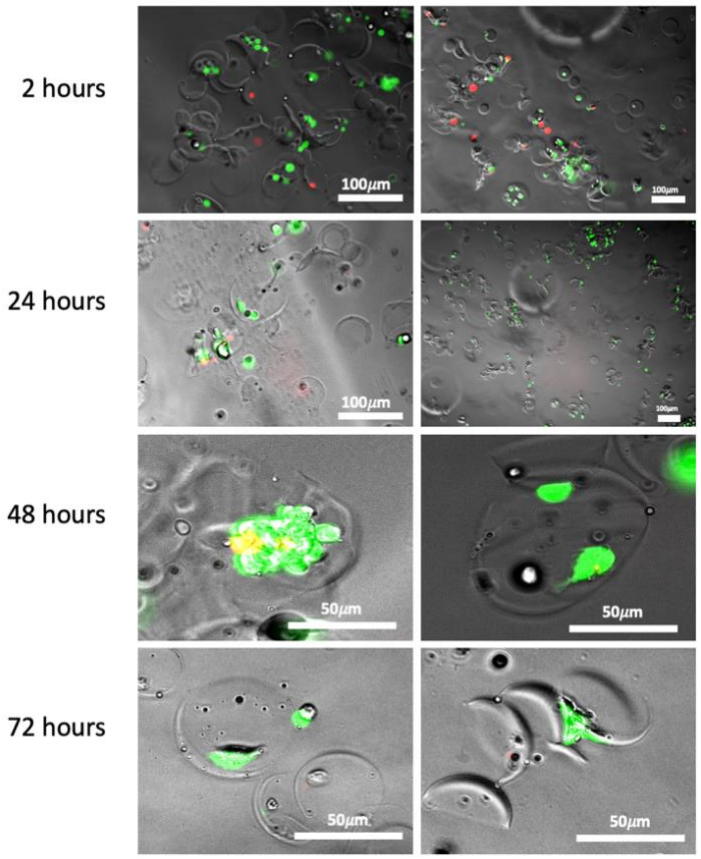

Figure 9. Live dead assay of GFP+Fibroblasts encapsulated in C3 CLP hydrogel microspheres. Live/dead staining assay showing the viability of encapsulated GFP-tagged Fibroblasts over 72 hours. Green fluorescence indicates live cells, while red fluorescence denotes dead or dying cells.

Subsequent microencapsulation experiments and data collection were conducted exclusively using the optimized C30 formulation, which demonstrated the highest reproducibility and efficacy in generating monodisperse microspheres with favorable biocompatibility for cell encapsulation.

To further evaluate encapsulated cell viability, a series of Live/Dead assays were performed over a 72-hour period using two biomaterial systems: agarose and C30-based microspheres. Green fluorescent protein (GFP)-expressing fibroblast-like cells (GFP^+ FBS) were encapsulated in both systems. Agarose served as the control, as its performance in microsphere-based encapsulation has been well-established by the Godin laboratory, owing to its stability, inertness, and minimal toxicity.

As shown in **Figure 10.A**, both agarose and C30 microspheres were successfully formed. While most C30 microspheres displayed uniform morphology, some showed folding or slight deformation, likely due to hydrogel swelling, which was more pronounced in the C30 formulation compared to the agarose-based microspheres. Despite these differences, both systems maintained structural integrity over the 72-hour incubation period.

Figure 10.B presents the quantitative analysis for the survival of encapsulated cells. At both 24 and 48 hours, no statistically significant difference in cell survival was observed between the two biomaterials, with both groups maintaining high viability rates (median survival >85%). However, by 72 hours, a significant difference in survival emerged between the two groups. C30 CLP microspheres preserved a higher proportion of viable cells (median ~90%), whereas agarose microspheres showed a notable decline in viability (median ~75%). Statistical analysis confirmed that the survival rate at 72 hours was significantly higher in C30 CLP microspheres compared to agarose ($p<0.01$). Throughout the assay, a small number of free-floating dead cells were occasionally observed in both systems. However, the overall frequency of these events remained low, suggesting that most cells remained stably encapsulated post-encapsulation and that the hydrogel matrices effectively retained cell populations during the observation period.

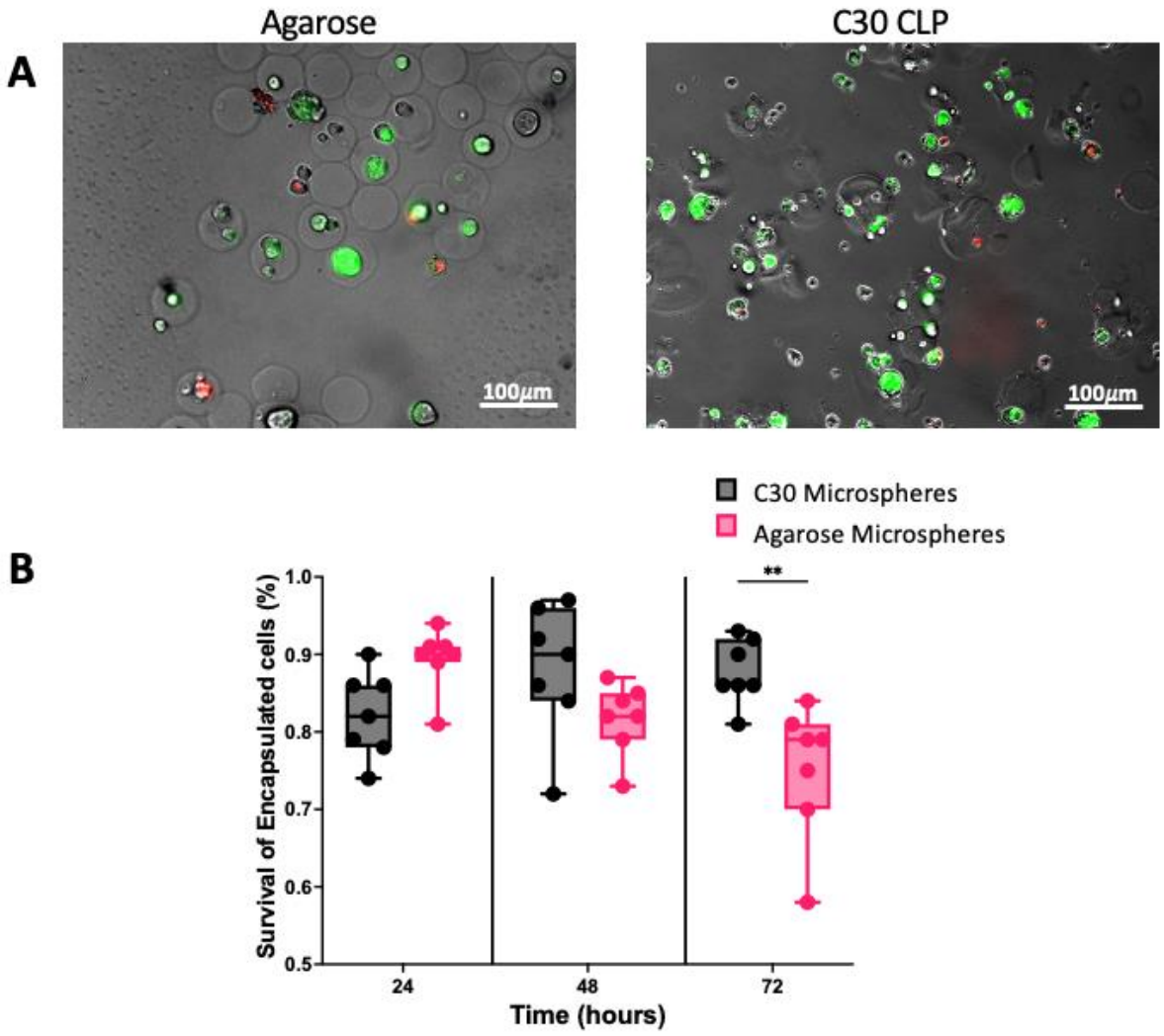

Figure 10. Live/dead assay of GFP+ fibroblasts encapsulated in C30 CLP and agarose hydrogel microspheres. Optimization of the C30 CLP hydrogel formulation improved microsphere formation and individual encapsulation. **A)** Left panel: Live/dead staining of GFP+ fibroblasts in agarose microspheres. Right panel: Live/dead staining of GFP+ fibroblasts in new sequence C30 CLP microspheres. **B)** Quantification of cell survival (%) over 24, 48, and 72 hours. ** as $p < 0.05$ indicates statistical significance.

The encapsulation efficiency of the C30 CLP microspheres was evaluated by calculating the proportion of total number of encapsulated cells over the total number of cells **Figure 11A**. As shown in **Figure 11B**, at both 24- and 48-hours post-encapsulation, agarose microspheres

exhibited significantly higher encapsulation efficiencies compared to C30 microspheres, with median values exceeding 80% for agarose and approximately 60% for C30. However, by 72 hours, the difference in encapsulation efficiency between the two biomaterials was no longer statistically significant. This convergence suggests that while C30 initially underperforms in cell occupancy relative to agarose, it maintains stable encapsulation over time, potentially indicating improved long-term retention.

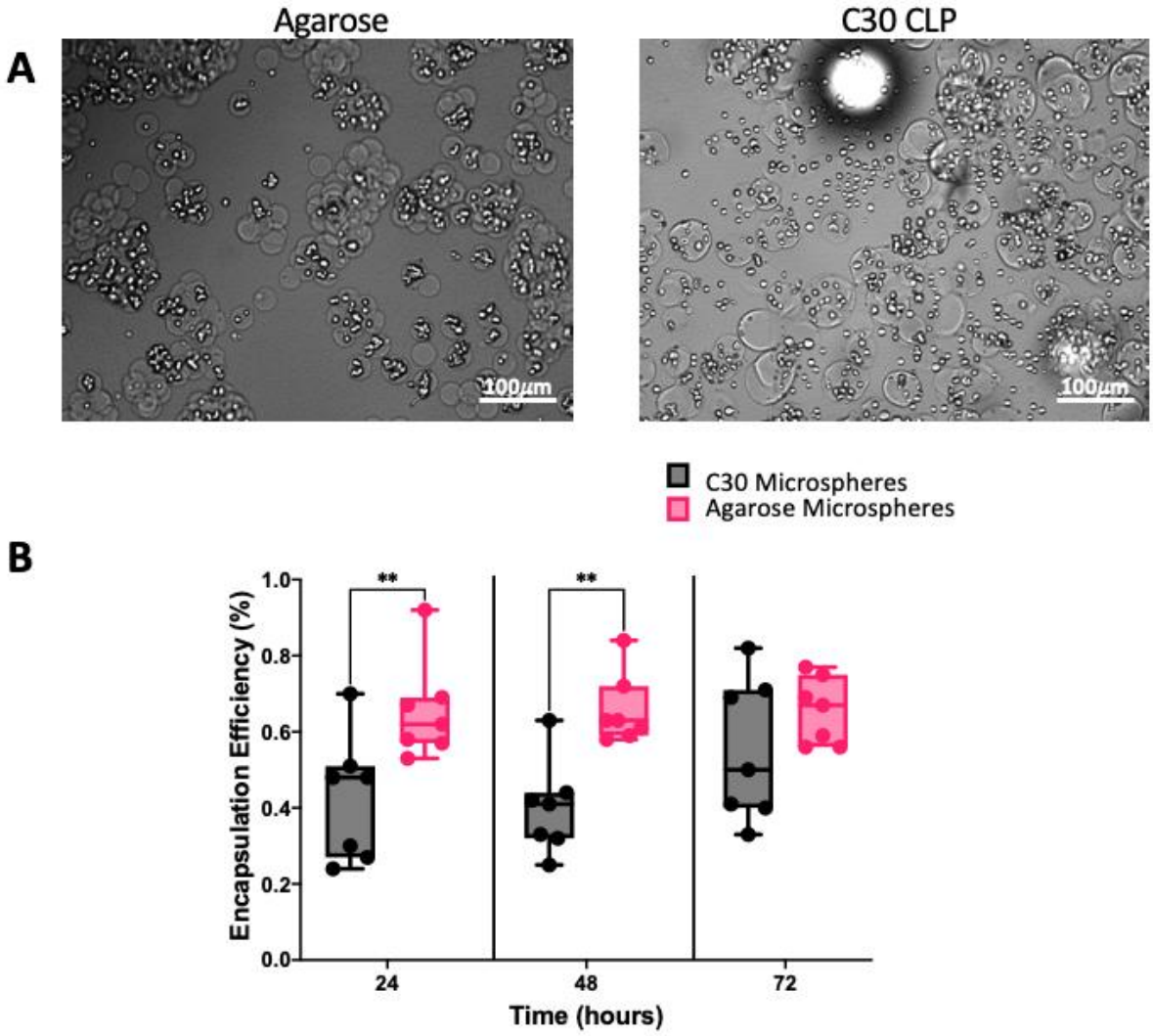

Figure 11. Evaluation of cell encapsulation efficiency in agarose and C30 CLP hydrogel microspheres. **A)** Brightfield images of agarose and C30 CLP microspheres containing encapsulated GFP+Fibroblast cells. **B)** Quantification graph showing encapsulation efficiency over 24, 48 and 72 hours. ** as $p < 0.05$ indicates statistical significance.

Characterization of Microspheres

The goal of this stage of experimentation was to characterize the mechanical properties of the generated hydrogel microspheres. This was done by preparing a new batch of cell-free microspheres. Scanning Electron Microscopy (SEM) was employed to visualize microsphere morphology and evaluate structural characteristics, including diameter and pore size (**Figure 12)**. Two different SEM sample preparation methods were explored to find the most optimal one for the material used. The first involved air-drying the microspheres followed by a plasma-induced gold atoms sputter-coating. However, this approach failed to preserve microsphere architecture, revealing only collapsed outer shells with no discernible internal features (**Supplementary Figure S3**). In contrast, the second method involving cryopreservation prior to imaging produced high-resolution images with well-defined microsphere morphology, enabling accurate visualization of surface and internal structures. SEM analysis confirmed that both agarose and C30 CLP microspheres maintained a consistent size range between 50–60 μm in diameter (**Figure 12**). Furthermore, the cryopreserved C30 microspheres revealed visible porous architecture, with pore diameters measured in the range of 0.5- 14 μm (**Figure 13**). The bar graph demonstrates a heterogeneity in pore size distribution, with most of the pores clustering between 1.4-2.8 μm. Data were collected from multiple microspheres across different fields of view to ensure representative sampling.

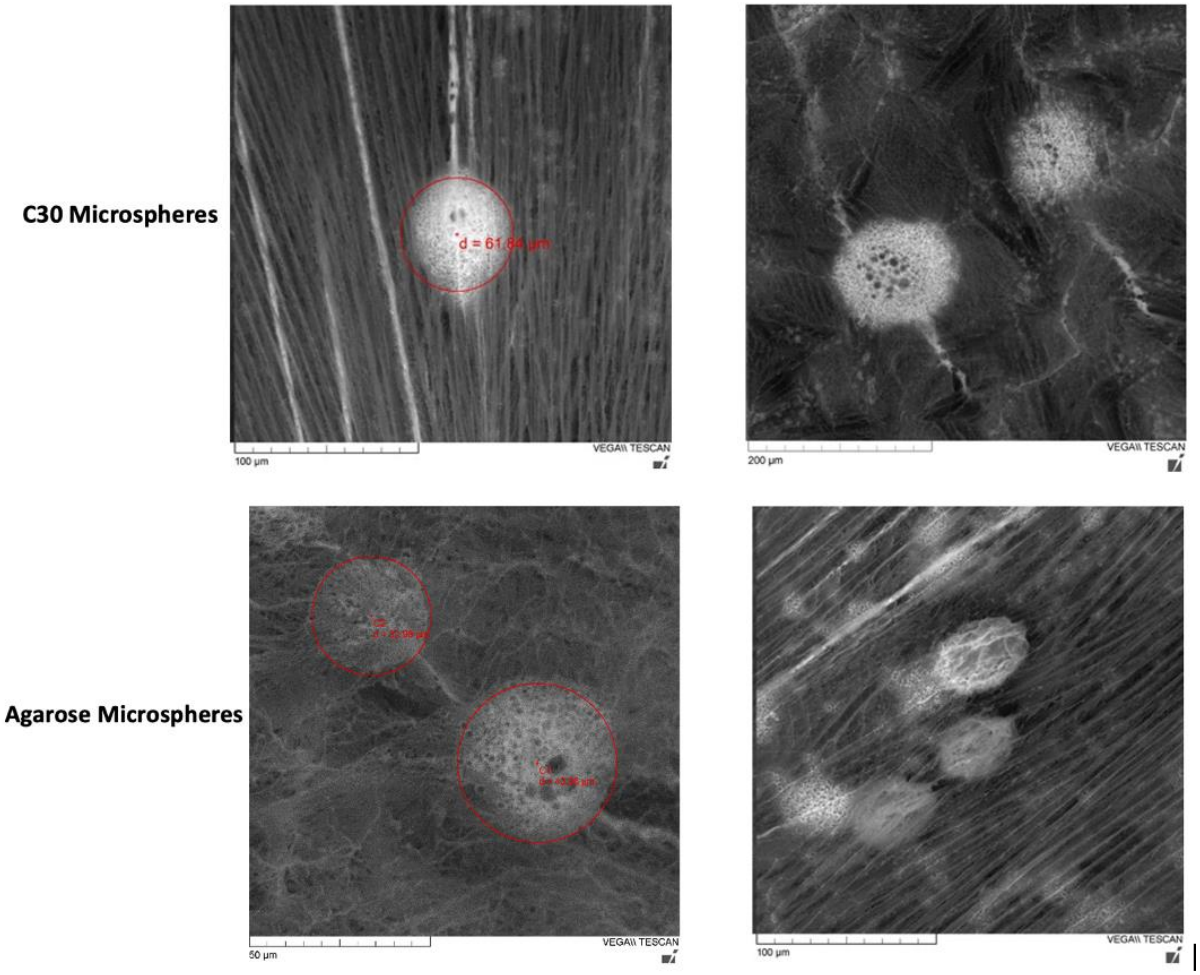

Figure 12. Scanning Electron Microscopy (SEM) of agarose and C30 CLP microspheres. SEM images of C30 CLP microspheres (left) and agarose microspheres (right), with microsphere circumference and with it, the diameter, indicated in red (µm).

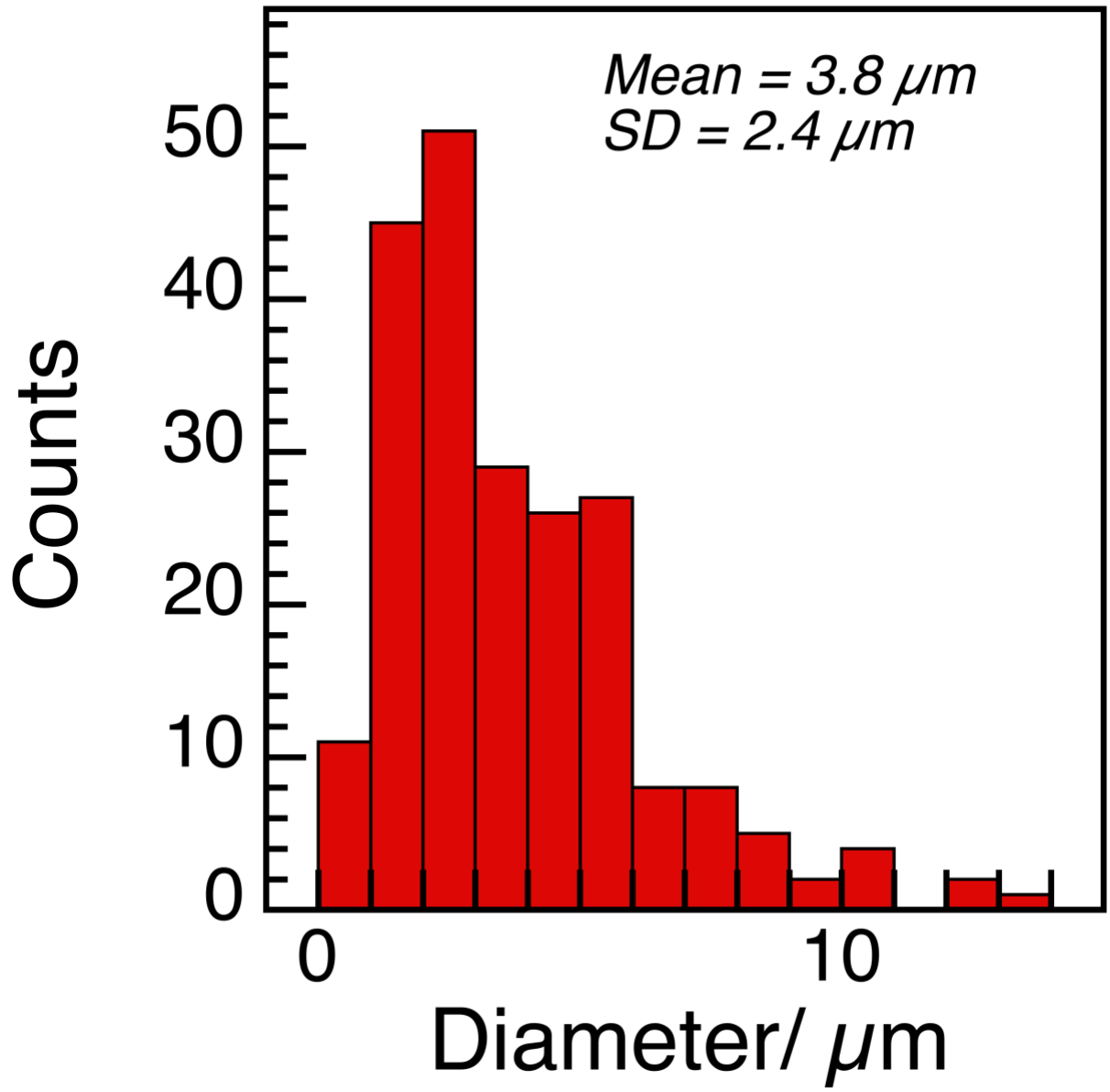

Figure 13. Quantification of pore size distribution in C30 microspheres. Bar graph illustrating the range and frequency of pore diameters (µm) observed in cryopreserved, cell-free C30 collagen-like peptide (CLP) microspheres imaged using scanning electron microscopy (SEM). Pore sizes were grouped into defined intervals (e.g., 1–2 µm, 2–3 µm, etc.), with each bar representing the number of pores falling within each size category.

To assess the enzymatic degradability of the hydrogels, a collagenase degradation assay was conducted. The degradation assay was carried out for both microsphere and bulk forms of the two hydrogels (C30 and agarose) and compared with a collagen hydrogel. As expected, agarose in both the microspheres and bulk form demonstrated resistance to enzymatic degradation over the testing period, consistent with the known stability of agarose in the presence of collagenase (**Figure 14 A and B**). In contrast, the residual mass of C30 CLP microspheres decreased gradually over time mirroring the behavior of collagen hydrogel (**Figure 14A**). As for bulk hydrogel collagenase testing, C30 showed progressive degradation when exposed to collagenase, but at a slower rate, owing to its bulk hydrogel nature (**Figure 14B**). These results indicate the enzymatically responsive nature of the C30 CLP material.

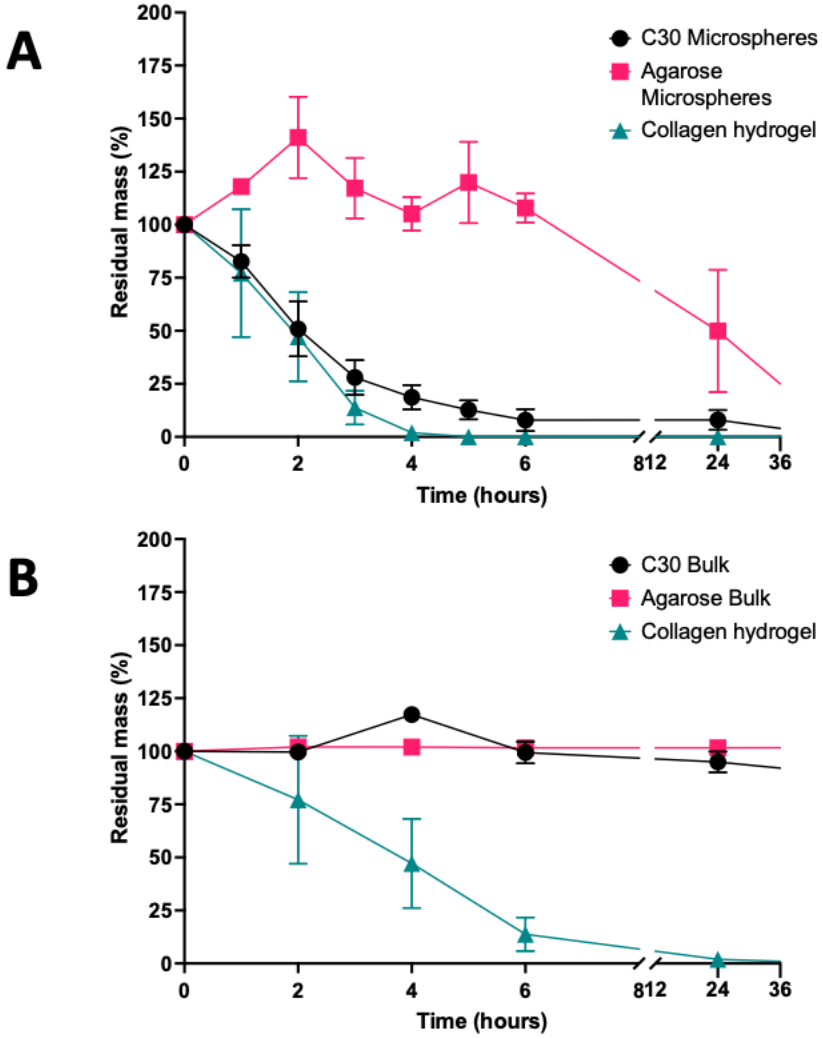

Figure 14. Collagenase degradation assay for both microspheres and bulk forms of CLP C30, agarose and collagen. A) The residual mass percentage of C30 microspheres, agarose microspheres, and collagen hydrogel, and **B)** C30 bulk, agarose bulk, and collagen hydrogel materials over a 36-hour period. The graphs illustrate the degradation behavior of each material when subjected to collagenase.

To complement the structural analysis of the microspheres, additional characterization tests were carried out to assess the physicochemical properties of the peptides used. Circular dichroism (CD) spectroscopy was performed to assess the secondary structure of the C3 and C30 collagen-like peptides at three different concentrations: 50 μM, 100 μM, and 200 μM. The CD spectra for both peptides revealed two distinct peaks: a positive peak around 225 nm and a negative peak near 200 nm. These characteristic signals are indicative of a polyproline type II helix, a conformation typical of collagen-mimetic structures. All spectra were recorded at 20 °C and pH 7.4 (**Figure 15.A**). Relative folding values (Rpn) calculated from the CD spectra showed that C30 exhibited slightly higher folding tendencies compared to C3 at all tested concentrations. Specifically, at 50 μM, Rpn was 0.0815 for C3 and 0.0858 for C30; at 100 μM, 0.0869 for C3 and 0.0906 for C30; and at 200 μM, 0.0873 for C3 and 0.0938 for C30 (**Figure 15.B**).

A

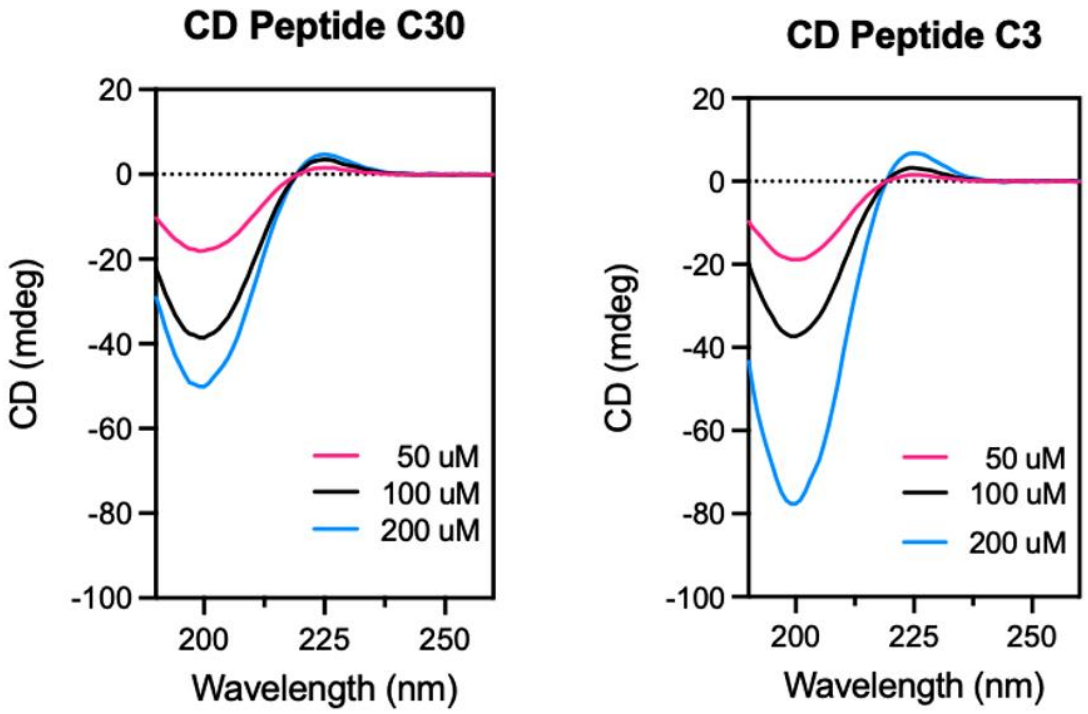

B

Rpn

Concentration (µM)	C3	C30
50	0.0815	0.0858
100	0.0869	0.0906
200	0.0873	0.0938

Figure 15. Circular Dichroism (CD) Spectra and Folding (Rpn) values of C30 and C3 peptides. **A)** CD spectra graphs of C30 and C3 peptides at concentrations of 50 µM, 100 µM, and 200 µM, showing concentration dependent changes in secondary structure characteristics. **B)** Table presents Folding (Rpn) values for C3 and C30 peptides at concentrations of 50 µM, 100 µM, and 200 µM. Experiments were carried out in phosphate saline buffer pH 7.4.

The melting temperature **(Table 3)** shows that C30 demonstrated a higher melting temperature (65°C) compared to C3 (59°C), although no significant difference exists between the two. Reference melting graphs can be found in **Supplementary Figure S4**.

Table 3. Comparison of melting temperatures (Tm) between C3 and C30 collagen-like peptides (CLPs). Tm values were determined by monitoring changes in ellipticity at 220 nm from 20°C to 75°C, indicating the thermal stability of each peptide.

Melting Temperature (Tm) ℃	
C3	**C30**
59.0 ± 3.0	65.0 ± 6.0

To further characterize the materials' physical properties, viscosity measurements were performed across increasing shear rates. At the working concentration of PEG-Mal (5 mM), the viscosity was found to be higher than that of the C30 peptide solution, consistent with expectations given its polymeric nature **(Supplementary Figure S1)**. Thermal characterization was performed using Differential Scanning Calorimetry (DSC). Results revealed that agarose exhibited a denaturation transition at approximately 90 °C, while no distinct thermal transitions were observed for either C3 or C30 over the temperature range tested, suggesting high thermal stability or gradual thermal unfolding. It is important to note that both agarose and C30 hydrogels possess high water content, which may contribute to the observed thermal behavior **(Supplementary Figure S5)**.

Infrared (IR) spectroscopy was also conducted to analyze the molecular structures of C3 and C30. The spectra revealed multiple characteristic peaks, including strong signals corresponding to amide I (~1650 cm^{-1}), amide II (~1550 cm^{-1}), and amide III (~1300 cm^{-1}), which are all associated with the peptide backbone and confirm the presence of peptide bonds. Additionally, broad OH and NH stretching bands were observed, further supporting the peptides' structural integrity and hydrogen-bonding potential. The presence of amide I, in particular, is indicative of defined secondary structure, reinforcing the collagen-like nature of both peptides **(Supplementary Figure S6)**.

Discussion

Tissue regeneration studies, particularly in the context of keratoconus, have witnessed major advancements. However, several limitations persist, especially with the direct injection of cells in suspension. Cell therapies are hampered by the lack of delivery systems resulting in inconsistent outcomes in animal studies and human clinical trials[140]. In vivo studies suggest that free cells injected into damaged tissue suffer from poor retention, low rates of engraftment [141,142], low viability, and limited therapeutic efficacy due to rapid clearance from the site of damage [141,143–145]. As such, the need for improved delivery vehicles and scaffolding materials for improving regenerative cell therapy is critical. While the corneal stroma is avascular and may not experience the same level of systemic clearance as other tissues, free-floating cells may not always distribute evenly, fail to integrate, or undergo apoptosis due to lack of mechanical support and detachment from the ECM (anoikis) and trophic cues[146–148]. Thus, effective cell retention remains a challenge, and the need for protective delivery platforms, such as biomaterial-based hydrogel scaffolds, is still critical for ensuring cell survival, localization, and long-term therapeutic benefit. Hydrogels offer the advantage of homogeneous distribution, protection, customizable properties to have specific chemical and mechanical properties to promote cell survival, proliferation, and differentiation, and can reduce the formation of corneal scars by providing scaffold for cell growth and integration [149].

Injectable hydrogels offer a promising alternative, not only to physically support and thicken the cornea but also to serve as carriers for stromal cells. These hydrogels provide a three-dimensional, ECM-like scaffold that can protect the encapsulated cells from environmental or mechanical stress, while also supporting their function, survival, and integration into host tissue [123]. Microfluidic-generated hydrogel microspheres present a unique opportunity by offering precise control over size, uniformity, and encapsulation efficiency. However, most prior work has focused on a limited set of biomaterials such as gelatin, alginate, and agarose, occasionally incorporating porcine cornea into alginate, limiting innovation in this field as we have discussed their disadvantages early on. Thus, appropriate polymers have not been adaptable to microsphere manufacturing for different reasons such as difficulty in forming hard hydrogels in a time efficient manner for example.

This study addresses two key gaps: (1) the underutilization of synthetic collagen-like peptides (CLPs) in microfluidic systems, and (2) the need for tunable, injectable scaffolds suitable for stromal regeneration in keratoconus. While CLPs have previously been used to thicken corneal stroma [93], this study is, to the best of our knowledge, the first to adapt such successful synthetic materials for cell encapsulation via microfluidic microsphere generation representing a novel intersection of peptide biomaterials and precision hydrogel engineering.

Our findings began with the optimization of a pre-developed CLP (C3) by modifying its sequence to improve compatibility with a microfluidic encapsulation system. C3 was found to form sparse microspheres, with many gels clumping or clogging the device due to its rapid gelation. Specifically, C3 contains 8 POG repeats and is among the sequences that gels fast from our library (33 ± 2 seconds) [93]. Its use in microfluidics produced very inconsistent results.

To counteract this, alternative sequences such as C35 (5 POG repeats, gels in 108 ±8 seconds), C3XF (7 POG + POV insert, gels in 24 ± 41 seconds), and C30 (10 POG repeats, gels in 47 ± 35 seconds) were explored. Interestingly, only C30 successfully formed uniform microspheres without clogging the system. C3XF is another sequence tested but failed to form microspheres. C3XF has the same number of amino acids as C3, but with a different folding behavior as it was forced to lose it due to having a POV sequence instead of POG. It is also important to note that the Rpn of C3XF is around 0.028, which is much lower than that of C3 and C30 which most closely resembles native collagen folding [93]. C3XF failed in forming microspheres, suggesting that the folding of the peptide plays a key role in forming microspheres. On the other hand, using C30 to make better microspheres could be related to a longer chain when compared to C35 and C3. It is important to note that all the optimizations to establish monodisperse droplet formation was done by tuning the peptide structure and optimizing different sequences. Additional tests could be done to establish a clear pattern on why exactly C30 performed better than the rest of the tested peptide sequences. However, these results emphasize that slower gelation kinetics, specific sequence, combined with specific surfactant (Span 80) conditions and PEG-Mal ratios, are critical for stable microfluidic encapsulation. The HLB (Hydrophile-Lipophile Balance) value of the surfactant used played a critical role in emulsion formation. Non-ionic surfactants are classified along the HLB scale, which predicts their behavior based on the relative molecular weights of their hydrophilic

and hydrophobic segments. Surfactants with higher HLB values are more hydrophilic and typically stabilize oil-in-water (O/W) emulsions, while those with lower HLB values are more lipophilic and favor water-in-oil (W/O) emulsions [150–153]. Achieving a stable emulsion in microfluidic systems requires balancing the stabilization of the droplets to prevent coalescence while maintaining monodispersity at higher flow rates. Span 80, the surfactant used in this study, has a low HLB value of 4.3, making it suitable for stabilizing W/O emulsions used here. Optimal droplet formation was achieved using 2% Span 80 in a 1:10 PEG-to-oil ratio.

To accommodate the gelation mechanism of the CLP-PEG system (via Michael addition between thiol and maleimide groups), the original Godin Lab microfluidic device was redesigned to introduce two additional PEG-Mal inlets, ensuring better mixing and reduced clogging, along with a series of changes including microchannel size and length optimizations. PEG was combined with Span 80 to address its high viscosity, improve flow stability, and monodispersity of microspheres. Cells were added to the CLP phase rather than the PEG-Mal phase, as some studies have suggested some potential cytotoxicity of PEG-Mal under certain conditions[154]. Our prior cytotoxicity testing confirmed that CLP is more compatible with cells, even at higher concentrations, whereas PEG-Mal demonstrated significant cytotoxicity **(Supplementary figure S9)**.

Encapsulation with C30 maintained high cell viability across time points (24h, 48h), and even outperformed agarose microspheres at 72h. Encapsulation efficiency of C30 was also like that of agarose, with agarose outperforming C30 at 24 to 48 hours but equating it at 72 hours. This suggests C30s structural and mechanical properties support cell survival. However, it is hard to tell why the encapsulation efficiency of agarose was better. Encapsulation efficiency was calculated by dividing the total number of encapsulated cells by the total number of cells. While the encapsulation efficiency of C30 is still great. It is possible that further optimizations are needed to improve the outcomes even more.

Cell loss from microspheres may be due to egress, when cells exit the hydrogel microsphere, which is difficult to track visually. Literature has shown that cells encapsulated in RGD-modified agarose can egress and adhere to the outside of microcapsules[155], possibly indicating a similar phenomenon in our study. Given that fewer cells appeared in agarose at 72h, we hypothesize that the egress rate

may differ between materials, warranting future migration studies assessing cellular migration out of the microspheres. In our case, regenerative medicine and tissue integration, cell egress is a favorable outcome, as our goal is to enable stromal repopulation of the cells. The microspheres serve as a temporary protective and supportive niche during injection, after which cells are expected to migrate out and integrate into the surrounding corneal tissue.

Another possibility related to cell egress is related to SEM analysis. This analysis revealed a heterogeneous pore structure in C30 microspheres (range 0.5- 14 μm) whereas agarose pores (~200–400 nm [156]) were not visible under the same conditions. C30's larger and visible pores may support improved nutrient exchange and cell viability. Literature suggests good pore sizes for fibroblast ingrowth and neovascularization inside hydrogels can start from a minimum of 5-15 μm, aligning with the porous nature observed in C30 [157]. Additionally, literature suggests that cell fate is influenced by hydrogel stiffness and network structure. Literature shows that stiffer hydrogels (e.g., PEGDA) limit migration and reduce viability, while softer, more permeable networks (e.g., acrylated hyaluronic acid) promote better viability and release (although viability was still not optimal in them after 1 week of encapsulation) [121,140]. C30's balance may lie closer to the latter, offering a more favorable microenvironment. In contrast, agarose lacks cell-adhesive properties, and microscopy showed minimal attempts by encapsulated cells to adhere or spread.

In terms of characterization properties, Circular dichroism (CD) showed that both C3 and C30 maintained triple-helical features. C30 had slightly higher Rpn values (0.085–0.093) than C3 (0.081–0.087), suggesting increased triple-helix content. Native collagen has an RPN of ~0.12 [158], placing C30's folding closer to physiologic collagen. Another characterization test, DSC, revealed that C30 had a slightly higher melting temperature (~65°C vs. ~59°C for C3). This refers to the energy needed to unfold the triple helical structure of CLP, meaning that the higher the temperature for unfolding, the stronger the interactions within the peptide. Although not significant, this could play a role in greater structural stability and stronger intramolecular interactions for C30. Additionally, FTIR spectra for C30 and C3 confirmed the presence of characteristic amide I, II, and III bands, OH and H, consistent with peptide secondary structures and triple-helix formation[93,158]. This served as another method to confirm the triple-helical collagen-mimetic structure of C30, while DSC and viscosity profiling demonstrated thermal and mechanical

stability, supporting its suitability for injectable applications. Collagenase assays demonstrated that agarose remained unchanged due to lack of collagenase-sensitive bonds which matches the literature, while both C3 and C30 showed gradual degradation, which is desirable mimicking the way native collagen degrades *in vivo*. Additionally, since the hydrogel contains both CLP and PEG, this is consistent with the literature as PEG is known for their slow degradation in vivo[159]. Notably, microspheres degraded faster than bulk hydrogels, possibly due to increased surface area and lower PEG shielding in the former. This also provides us with the possibility to control our material's degradation rate based on their size, which could be beneficial for future control of degradation.

By integrating rational peptide design with microfluidic encapsulation, this study demonstrates a novel approach for corneal tissue regeneration. The dual function of C30, biomimicry of native tissue and cell encapsulation, positions it as a potential therapeutic vehicle for Keratoconus and other stromal pathologies. The findings contribute to ongoing efforts to expand the biomaterial library for microfluidics and demonstrate that synthetic peptides can achieve reproducible, tunable, and biocompatible microspheres.

Importantly, this strategy offers several advantages over bulk gelation, including controlled size distribution, improved cell encapsulation efficiency, and better injectability. Additionally, the use of a synthetic peptide allows for precise sequence control, avoiding batch variability and immunogenicity concerns of animal-derived collagen.

This study has several limitations. First, the microfluidic system operates on small volumes, limiting throughput. Scale-up strategies, such as parallelized chips or continuous flow systems, should be explored. Second, encapsulated cells were only tracked over 72 hours, which is insufficient to determine long-term behavior or regenerative potential. Another limitation is the swelling behavior of the C30 microspheres compared to agarose. Although the microsphere size was controlled for both CLP and agarose, the CLP microspheres ended up a bit larger in size possibly due to swelling.

Although live/dead assays were favorable, in vivo immune response remains unknown. While C30 and PEG showed no cytotoxicity in vitro, their long-term fate, potential degradation products, and

immunogenicity in ocular tissues must be studied. Future work should evaluate host integration, stromal remodeling, and foreign body responses in animal models.

Additionally, tuning crosslinking density, incorporating pro-regenerative signals (e.g., growth factors), and engineering specific release kinetics may further optimize outcomes. Longer-term culture and egress tracking studies are essential to confirm migration patterns and cell fate.

This study is the first to demonstrate the use of synthetic collagen-like peptides for generating cell-laden hydrogel microspheres using microfluidics for potential application in corneal stromal regeneration. Through careful peptide design and device optimization, a biocompatible and effective encapsulation system was developed. These results provide a strong foundation for future translational research in regenerative ophthalmology and contribute to the broader field of peptide-based biomaterials in precision medicine.

Conclusion

This thesis explored the development of hydrogel microspheres using an optimized collagen-like peptide (CLP) material as a platform for cell encapsulation and delivery. Cell therapy often relies on injecting cells in suspension, but this approach comes with challenges such as poor survival, weak integration, and limited long-term effectiveness. Many studies have shown that delivering cells within biomaterial-based scaffolds improves their viability and therapeutic potential. In this work, we extended the application of CLP hydrogels from our peptide library, optimized its formulation to apply for beyond bulk tissue injections and demonstrated its potential as a microsphere-based cell carrier.

One of the biggest hurdles in microfluidics is the limited range of biomaterials available for microsphere generation. Expanding this library is crucial, and by optimizing the formulation and sequence of our pre-developed CLP-based hydrogel, we aimed to contribute to this growing field. This project tackled key challenges in cell delivery, tissue repair, and microfluidic encapsulation by systematically fine-tuning microsphere generation parameters, characterizing their chemical and physical properties, and validating their performance through *in vivo* studies. Our results not only confirmed that our CLP hydrogels can be adapted into microspheres for cell encapsulation but also highlighted their tunability in size, porosity, adhesivity, and bioactivity through peptide sequence and formulation modifications.

Looking ahead, future studies should explore how encapsulated cells migrate out of the microspheres and behave in biomimetic synthetic tissues like corneal stroma, skin, and heart models. Another important step will be designing a microfluidic system for large-scale, automated, consistent, and high-throughput microspheres production, reducing variability, optimizing flow rates and pressures automatically without the need for constant human intervention and optimization during the microfluidic run itself. Addressing these challenges will bring us closer to making CLP microspheres a viable tool for regenerative medicine and cell-based therapies. Beyond these direct applications, this research contributes to the broader field of regenerative medicine by demonstrating how synthetic biomaterials can be leveraged for more efficient, scalable cell therapies. By integrating microfluidic technologies with bioengineered hydrogels, this

work lays the foundation for the development of next-generation biomaterials that offer greater control over cell delivery and tissue regeneration.

References

1. Fan, L., Kandel, H. & Watson, S. L. Impacts of keratoconus on quality of life: a qualitative study. *Eye* **38**, 3136–3144 (2024).
2. Aghamohammadzadeh, H., Newton, R. H. & Meek, K. M. X-ray scattering used to map the preferred collagen orientation in the human cornea and limbus. *Structure* **12**, 249–256 (2004).
3. 2.6: The Eye. *Physics LibreTexts* (2016).
4. DelMonte, D. W. & Kim, T. Anatomy and physiology of the cornea. *J Cataract Refract Surg* **37**, 588–598 (2011).
5. Remington, L. A. Chapter 2 - Cornea and Sclera. in *Clinical Anatomy and Physiology of the Visual System (Third Edition)* (ed. Remington, L. A.) 10–39 (Butterworth-Heinemann, Saint Louis, 2012). doi:10.1016/B978-1-4377-1926-0.10002-5.
6. Binder, P. S., Rock, M. E., Schmidt, K. C. & Anderson, J. A. High-voltage electron microscopy of normal human cornea. *Invest Ophthalmol Vis Sci* **32**, 2234–2243 (1991).
7. Tkachev, S. Y. *et al.* Visualization of different anatomical parts of the enucleated human eye using X-ray micro-CT imaging. *Exp Eye Res.* **203**, 108394 (2021).
8. Pineda, R. World Corneal Blindness. 299–305 (2020) doi:10.1007/978-3-030-25335-6_25.
9. Gain, P. *et al.* Global Survey of Corneal Transplantation and Eye Banking. *JAMA Ophthalmology* **134**, 167–173 (2016).
10. Hashemi, H. *et al.* The Prevalence and Risk Factors for Keratoconus: A Systematic Review and Meta-Analysis. *Cornea* **39**, 263–270 (2020).
11. Kennedy, R. H., Bourne, W. M. & Dyer, J. A. A 48-Year Clinical and Epidemiologic Study of Keratoconus. *Am J Ophthalmol.* **101**, 267–273 (1986).

12. Godefrooij, D. A., de Wit, G. A., Uiterwaal, C. S., Imhof, S. M. & Wisse, R. P. L. Age-specific Incidence and Prevalence of Keratoconus: A Nationwide Registration Study. *Am J Ophthalmol.* **175**, 169–172 (2017).

13. Prevalence and incidence of keratoconus in Norway: a nationwide register study - Kristianslund - 2021 - Acta Ophthalmologica - Wiley Online Library. https://onlinelibrary-wiley-com.proxy.bib.uottawa.ca/doi/full/10.1111/aos.14668.

14. Rabinowitz, Y. S. Keratoconus. *Surv Ophthalmol.* **42**, 297–319 (1998).

15. Rebenitsch, R. L., Kymes, S. M., Walline, J. J. & Gordon, M. O. The Lifetime Economic Burden of Keratoconus: A Decision Analysis Using a Markov Model. *Am J Ophthalmol.* **151**, 768-773.e2 (2011).

16. Singh, R. B., Parmar, U. P. S. & Jhanji, V. Prevalence and Economic Burden of Keratoconus in the United States. *Am J Ophthalmol.* **259**, 71–78 (2024).

17. Leung, V. C., Pechlivanoglou, P., Chew, H. F. & Hatch, W. Corneal Collagen Cross-Linking in the Management of Keratoconus in Canada: A Cost-Effectiveness Analysis. *Ophthalmology* **124**, 1108–1119 (2017).

18. Nguyen, M. The cost of vision loss and blindness in Canada.

19. Kristianslund, O. & Drolsum, L. Prevalence of keratoconus in persons with Down syndrome: a review. *BMJ Open Ophth* **6**, e000754 (2021).

20. C, P., Babitha, V., Prabhu, P. B. & P.t, J. Comparison of Topographic and Biomicroscopic Features Among Symptomatic Keratoconic Eyes. *The Off Sci J Delhi Ophthalmol Soc*. **29**, 44–48 (2018).

21. Fransen, E. *et al.* Resequencing of candidate genes for Keratoconus reveals a role for Ehlers–Danlos Syndrome genes. *Eur J Hum Genet* **29**, 1745–1755 (2021).

22. Mackiewicz, Z. *et al.* Collagenolytic Proteinases in Keratoconus. *Cornea* **25**, 603–610 (2006).

23. Romero-Jiménez, M., Santodomingo-Rubido, J. & Wolffsohn, J. S. Keratoconus: A review. *Cont Lens Anterior Eye.* **33**, 157–166 (2010).

24. Meek, K. M. *et al.* Changes in Collagen Orientation and Distribution in Keratoconus Corneas. *Invest Ophthalmol Vis Sci.* **46**, 1948–1956 (2005).

25. Chen, S., Mienaltowski, M. J. & Birk, D. E. Regulation of corneal stroma extracellular matrix assembly. *Exp Eye Res* **133**, 69–80 (2015).

26. Meek, K. M. & Holmes, D. F. Interpretation of the electron microscopical appearance of collagen fibrils from corneal stroma. *Inter J Biol Macromol.* **5**, 17–25 (1983).

27. Singh, A., Maurya, O. P. S., Jagannadhan, M. V. & Patel, A. Matrix metalloproteinases (MMP-2 and MMP-9) activity in corneal ulcer and ocular surface disorders determined by gelatin zymography. *J Ocul Biol Dis Infor* **5**, 31–35 (2012).

28. Shetty, R. *et al.* Elevated expression of matrix metalloproteinase-9 and inflammatory cytokines in keratoconus patients is inhibited by cyclosporine A. *Invest Ophthalmol Vis Sci* **56**, 738–750 (2015).

29. Kim, W.-J., Rabinowitz, Y. S., Meisler, D. M. & Wilson, S. E. Keratocyte Apoptosis Associated with Keratoconus. *Exp. Eye Res.* **69**, 475–481 (1999).

30. Edrington, T. B. *et al.* Rigid contact lens fitting relationships in keratoconus. Collaborative Longitudinal Evaluation of Keratoconus (CLEK) Study Group. *Optom Vis Sci* **76**, 692–699 (1999).

31. Barraquer, J. I. Modification of refraction by means of intracorneal inclusions. *Int Ophthalmol Clin* **6**, 53–78 (1966).

32. Deshmukh, R. *et al.* Management of keratoconus: an updated review. *Front Med (Lausanne)* **10**, 1212314 (2023).

33. Elalfy, M. *et al.* Clinical outcomes after intracorneal ring segment implantation for keratoconus management in corneas with mild apical haze. *Ther Adv Ophthalmol* **13**, 25158414211003378 (2021).

34. Chan, C. Corneal Cross-Linking for Keratoconus: Current Knowledge and Practice and Future Trends. *Asia Pac J Ophthalmol (Phila)* **9**, 557–564 (2020).

35. Wittig-Silva, C. *et al.* A randomized controlled trial of corneal collagen cross-linking in progressive keratoconus: preliminary results. *J Refract Surg* **24**, S720-725 (2008).

36. McCall, A. S. *et al.* Mechanisms of Corneal Tissue Cross-linking in Response to Treatment with Topical Riboflavin and Long-Wavelength Ultraviolet Radiation (UVA). *Invest Ophthalmol Vis Sci* **51**, 129–138 (2010).

37. Caporossi, A., Baiocchi, S., Mazzotta, C., Traversi, C. & Caporossi, T. Parasurgical therapy for keratoconus by riboflavin-ultraviolet type A rays induced cross-linking of corneal collagen: preliminary refractive results in an Italian study. *J Cataract Refract Surg* **32**, 837–845 (2006).

38. Caporossi, A., Mazzotta, C., Baiocchi, S. & Caporossi, T. Long-term results of riboflavin ultraviolet a corneal collagen cross-linking for keratoconus in Italy: the Siena eye cross study. *Am J Ophthalmol* **149**, 585–593 (2010).

39. Subasinghe, S. K., Ogbuehi, K. C. & Dias, G. J. Current perspectives on corneal collagen crosslinking (CXL). *Graefes Arch Clin Exp Ophthalmol* **256**, 1363–1384 (2018).

40. Ruiz-Lozano, R. E., Gomez-Elizondo, D. E., Colorado-Zavala, M. F., Loya-Garcia, D. & Rodriguez-Garcia, A. Update on indications, complications, and outcomes of scleral contact lenses. *Med Hypothesis Discov Innov Ophthalmol* **10**, 165–178 (2022).

41. Zhang, X.-H. & Li, X. Effect of rigid gas permeable contact lens on keratoconus progression: a review. *Int J Ophthalmol* **13**, 1124–1131 (2020).

42. Sakellaris, D. *et al.* Intracorneal Ring Segment Implantation in the Management of Keratoconus: An Evidence-Based Approach. *Ophthalmol Ther* **8**, 5–14 (2019).

43. ICRS (Intracorneal Ring Segments) for Keratoconus. https://www.allan.vu/procedures/keratoconus/icrs/.

44. Baptista, P. M., Marques, J. H., Neves, M. M., Gomes, M. & Oliveira, L. Asymmetric Thickness Intracorneal Ring Segments for Keratoconus. *Clin Ophthalmol* **14**, 4415–4421 (2020).

45. Vega-Estrada, A., Chorro, E., Sewelam, A. & Alio, J. L. Clinical Outcomes of a New Asymmetric Intracorneal Ring Segment for the Treatment of Keratoconus. *Cornea* **38**, 1228–1232 (2019).

46. Agarwal, R., Jain, P. & Arora, R. Complications of corneal collagen cross-linking. *Indian J Ophthalmol* **70**, 1466–1474 (2022).

47. Cruz, G. K. P. *et al.* Clinical and surgical factors and intraoperative complications in patients who underwent penetrating keratoplasty. *Rev Lat Am Enfermagem* **27**, e3141.

48. Power, B. J. & Power, W. J. Penetrating Keratoplasty and Complications Management. in *Albert and Jakobiec's Principles and Practice of Ophthalmology* (eds. Albert, D. M., Miller, J. W., Azar, D. T. & Young, L. H.) 513–531 (Springer , Cham, 2022). doi:10.1007/978-3-030-42634-7_220.

49. Ferraz, M. P. Biomaterials for Ophthalmic Applications. *Appl. Sci.* **12**, 5886 (2022).

50. Winterton, L. C., Lally, J. M., Sentell, K. B. & Chapoy, L. L. The elution of poly (vinyl alcohol) from a contact lens: The realization of a time release moisturizing agent/artificial tear. *J Biomed Mater Res B: Appl Biomater.***80B**, 424–432 (2007).

51. Powell, C. H., Lally, J. M., Hoong, L. D. & Huth, S. W. Lipophilic versus hydrodynamic modes of uptake and release by contact lenses of active entities used in multipurpose solutions. *Cont Lens Anterior Eye.* **33**, 9–18 (2010).

52. Wu, K. Y., Qian, S. Y., Faucher, A. & Tran, S. D. Advancements in Hydrogels for Corneal Healing and Tissue Engineering. *Gels* **10**, 662 (2024).

53. Majcher, M. J. & Hoare, T. *Functional Biopolymers*. vols 453–490 (Springer International Publishing, Germany, 2019).

54. Ho, T.-C. *et al.* Hydrogels: Properties and Applications in Biomedicine. *Molecules* **27**, 2902 (2022).

55. Ahmad, Z. *et al.* Versatility of Hydrogels: From Synthetic Strategies, Classification, and Properties to Biomedical Applications. *Gels* **8**, 167 (2022).

56. Li, X., Sun, Q., Li, Q., Kawazoe, N. & Chen, G. Functional Hydrogels With Tunable Structures and Properties for Tissue Engineering Applications. *Front Chem* **6**, 499 (2018).

57. Ghosh, S. *et al.* Harnessing the power of biological macromolecules in hydrogels for controlled drug release in the central nervous system: A review. *Int J Biol Macromol.***254**, 127708 (2024).

58. Nicolson, P. C. & Vogt, J. Soft contact lens polymers: an evolution. *Biomaterials* **22**, 3273–3283 (2001).

59. Reddy, M. S. B., Ponnamma, D., Choudhary, R. & Sadasivuni, K. K. A Comparative Review of Natural and Synthetic Biopolymer Composite Scaffolds. *Polymers (Basel)* **13**, 1105 (2021).

60. Troy, E., Tilbury, M. A., Power, A. M. & Wall, J. G. Nature-Based Biomaterials and Their Application in Biomedicine. *Polymers (Basel)* **13**, 3321 (2021).

61. Liu, S. *et al.* Biomimetic natural biomaterials for tissue engineering and regenerative medicine: new biosynthesis methods, recent advances, and emerging applications. *Mil Med Res* **10**, 16 (2023).

62. Singh, G. & Chanda, A. Mechanical properties of whole-body soft human tissues: a review - IOPscience. *Biomedical Materials* https://iopscience-iop-org.proxy.bib.uottawa.ca/article/10.1088/1748-605X/ac2b7a/meta.

63. Ganewatta, M. S., Wang, Z. & Tang, C. Chemical syntheses of bioinspired and biomimetic polymers toward biobased materials. *Nat Rev Chem* **5**, 753–772 (2021).

64. Pascual-Gil, S., Garbayo, E., Díaz-Herráez, P., Prosper, F. & Blanco-Prieto, M. J. Heart regeneration after myocardial infarction using synthetic biomaterials. *J Control Release.* **203**, 23–38 (2015).

65. Scherzer, T., Beckert, A., Langguth, H., Rummel, S. & Mehnert, R. Electron beam curing of methacrylated gelatin. I. Dependence of the degree of crosslinking on the irradiation dose. *J Appl Polymer Sci.* **63**, 1303–1312 (1997).

66. Li, Y. & Wang, Z. Biomaterials for Corneal Regeneration. doi:10.1002/advs.202408021.

67. Chi, M., Yuan, B., Xie, Z. & Hong, J. The Innovative Biomaterials and Technologies for Developing Corneal Endothelium Tissue Engineering Scaffolds: A Review and Prospect. *Bioengineering (Basel)* **10**, 1284 (2023).

68. Delaey, J. *et al.* Tissue engineered scaffolds for corneal endothelial regeneration: a material's perspective. *Biomater. Sci.* **10**, 2440–2461 (2022).

69. Rafat, M. *et al.* PEG-stabilized carbodiimide crosslinked collagen-chitosan hydrogels for corneal tissue engineering. *Biomaterials* **29**, 3960–3972 (2008).

70. El-Sherbiny, I. M. & Yacoub, M. H. Hydrogel scaffolds for tissue engineering: Progress and challenges. *Glob Cardiol Sci Pract* **2013**, 316–342 (2013).

71. Hubbell, J. A. Materials as morphogenetic guides in tissue engineering. *Curr Opin Biotechnol.***14**, 551–558 (2003).

72. Lutolf, M. P. & Hubbell, J. A. Synthetic biomaterials as instructive extracellular microenvironments for morphogenesis in tissue engineering. *Nat Biotechnol* **23**, 47–55 (2005).

73. Kirchhof, S., Goepferich, A. M. & Brandl, F. P. Hydrogels in ophthalmic applications. *Eur J Pharm Biopharm.* **95**, 227–238 (2015).

74. Ding, X. *et al.* Synthetic peptide hydrogels as 3D scaffolds for tissue engineering. *Adv Drug Deliv Rev.* **160**, 78–104 (2020).

75. Liu, X. *et al.* Functionalized self-assembling peptide nanofiber hydrogels mimic stem cell niche to control human adipose stem cell behavior in vitro. *Acta Biomater.* **9**, 6798–6805 (2013).

76. Green, H., Ochbaum, G., Gitelman-Povimonsky, A., Bitton, R. & Rapaport, H. RGD-presenting peptides in amphiphilic and anionic β-sheet hydrogels for improved interactions with cells. *RSC Adv.* **8**, 10072–10080 (2018).

77. Duan, X. & Sheardown, H. Dendrimer crosslinked collagen as a corneal tissue engineering scaffold: Mechanical properties and corneal epithelial cell interactions. *Biomaterials* **27**, 4608–4617 (2006).

78. Caplan, M. R., Schwartzfarb, E. M., Zhang, S., Kamm, R. D. & Lauffenburger, D. A. Control of self-assembling oligopeptide matrix formation through systematic variation of amino acid sequence. *Biomaterials* **23**, 219–227 (2002).

79. Elsawy, M. A. *et al.* Controlling Doxorubicin Release from a Peptide Hydrogel through Fine-Tuning of Drug–Peptide Fiber Interactions. *Biomacromolecules* **23**, 2624–2634 (2022).

80. Bax, D. V. *et al.* Fundamental insight into the effect of carbodiimide crosslinking on cellular recognition of collagen-based scaffolds. *Acta Biomater.* **49**, 218–234 (2017).

81. Albrecht, W. N. & Stephenson, R. L. Health hazards of tertiary amine catalysts. *Scand J Work, Environ Health*. **14**, 209–219 (1988).

82. Li, S. *et al.* In vitro biocompatibility study of EDC/NHS cross-linked silk fibroin scaffold with olfactory ensheathing cells. *J Biomater Sci, Polym Ed.* **34**, 482–496 (2023).

83. Hennink, W. E. & van Nostrum, C. F. Novel crosslinking methods to design hydrogels. *Adv Drug Deliv Rev.* **54**, 13–36 (2002).

84. Lutolf, M. p., Raeber, G. p., Zisch, A. h., Tirelli, N. & Hubbell, J. a. Cell-Responsive Synthetic Hydrogels. *Adv Mater.* **15**, 888–892 (2003).

85. Diaferia, C. *et al.* The Introduction of a Cysteine Residue Modulates The Mechanical Properties of Aromatic-Based Solid Aggregates and Self-Supporting Hydrogels. *Chemistry.* **27**, 14886–14898 (2021).

86. Seow, W. Y., Salgado, G., Lane, E. B. & Hauser, C. A. E. Transparent crosslinked ultrashort peptide hydrogel dressing with high shape-fidelity accelerates healing of full-thickness excision wounds. *Sci Rep* **6**, 32670 (2016).

87. Islam, M. M. *et al.* Self-assembled collagen-like-peptide implants as alternatives to human donor corneal transplantation. *RSC Adv.* **6**, 55745–55749 (2016).

88. Kubyshkin, V. Stabilization of the triple helix in collagen mimicking peptides. *Org. Biomol. Chem.* **17**, 8031–8047 (2019).

89. Stawikowski, M. & Fields, G. B. Introduction to Peptide Synthesis. *Curr Protoc Protein Sci*, Unit-18.1 (2002).

90. Fagerholm, P. *et al.* A Biosynthetic Alternative to Human Donor Tissue for Inducing Corneal Regeneration: 24-Month Follow-Up of a Phase 1 Clinical Study. *Sci Trans Med*. **2**, 46ra61-46ra61 (2010).

91. McTiernan, C. D. *et al.* LiQD Cornea: Pro-regeneration collagen mimetics as patches and alternatives to corneal transplantation. *Sci Adv* **6**, eaba2187 (2020).

92. Uzunalli, G. *et al.* Bioactive self-assembled peptide nanofibers for corneal stroma regeneration. *Acta Biomater.* **10**, 1156–1166 (2014).

93. Ross, A. *et al.* Multipurpose On-the-Spot Peptide-Based Hydrogels for Skin, Cornea, and Heart Repair. *Adv Funct Mater*.**34**, (2024).

94. Cheng, S. *et al.* Features of S-nitrosylation based on statistical analysis and molecular dynamics simulation: cysteine acidity, surrounding basicity, steric hindrance and local flexibility. *Mol. BioSyst.* **10**, 2597–2606 (2014).

95. McGraw, T. Safety of polyethylene glycol 3350 solution in chronic constipation: randomized, placebo-controlled trial. *Clin Exp Gastroenterol.* **9**, 173–180 (2016).

96. Cooper, C. E. *et al.* Stability of Maleimide-PEG and Mono-Sulfone-PEG Conjugation to a Novel Engineered Cysteine in the Human Hemoglobin Alpha Subunit. *Front. Chem.* **9**, (2021).

97. Robins, S. P. Biochemistry and functional significance of collagen cross-linking. *Biochem Soc Trans.* **35**, 849–852 (2007).

98. Nair, D. P. *et al.* The Thiol-Michael Addition Click Reaction: A Powerful and Widely Used Tool in Materials Chemistry. *Chem. Mater.* **26**, 724–744 (2014).

99. Fontaine, S. D., Reid, R., Robinson, L., Ashley, G. W. & Santi, D. V. Long-Term Stabilization of Maleimide–Thiol Conjugates. *Bioconjugate Chem.* **26**, 145–152 (2015).

100. Fini, M. E., Yue, B. Y. J. T. & Sugar, J. Collagenolytic/gelatinolytic metatloproteinases in normal and keratoconus corneas. *Curr Eye Res.* (1992) doi:10.3109/02713689209033483.

101. Kao, W. W.-Y., Vergnes, J.-P., Ebert, J., Sundar-Raj, C. V. & Brown, S. I. Increased collagenase and gelatinase activities in keratoconus. *Biochem Biophys Res Comm*un.**107**, 929–936 (1982).

102. Dou, S., Liu, X., Shi, W. & Gao, H. New dawn for keratoconus treatment: potential strategies for corneal stromal regeneration. *Stem Cell Res Ther* **14**, 317 (2023).

103. Kitazawa, K., Sotozono, C. & Kinoshita, S. Current Advancements in Corneal Cell–Based Therapy. *Asia-Pac J Ophthalmol*. **11**, 335–345 (2022).

104. Soma, T. *et al.* Induced pluripotent stem-cell-derived corneal epithelium for transplant surgery: a single-arm, open-label, first-in-human interventional study in Japan. *The Lancet* **404**, 1929–1939 (2024).

105. Alió del Barrio, J. L. & Alió, J. L. Cellular therapy of the corneal stroma: a new type of corneal surgery for keratoconus and corneal dystrophies. *Eye Vis (Lond)* **5**, 28 (2018).

106. binte M. Yusoff, N. Z., Riau, A. K., Yam, G. H. F., binte Halim, N. S. H. & Mehta, J. S. Isolation and Propagation of Human Corneal Stromal Keratocytes for Tissue Engineering and Cell Therapy. *Cells* **11**, 178 (2022).

107. Yam, G. H.-F. *et al.* Safety and Feasibility of Intrastromal Injection of Cultivated Human Corneal Stromal Keratocytes as Cell-Based Therapy for Corneal Opacities. *Invest Ophthalmol Vis Sci.***59**, 3340–3354 (2018).

108. Ghiasi, M., Hashemi, M., Salimi, A., Tavallaie, M. & Aghamollaei, H. Isolation, Culture, Optimization and Validation of Human Corneal Stromal Keratocytes from Discarded Corneal Tissue. *J Appl Biotechnol. Rep.* **10**, 910–917 (2023).

109. Ahadi, M., Ramin, S., Abbasi, A., Tahmouri, H. & Hosseini, S. B. Mini review: human clinical studies of stem cell therapy in keratoconus. *BMC Ophthalmol* **24**, 35 (2024).

110. Alió del Barrio, J. L. *et al.* Cellular Therapy With Human Autologous Adipose-Derived Adult Stem Cells for Advanced Keratoconus. *Cornea* **36**, 952 (2017).

111. El Zarif, M. *et al.* Corneal Stromal Regeneration: A Review of Human Clinical Studies in Keratoconus Treatment. *Front Med (Lausanne)* **8**, 650724 (2021).

112. Ramin, S., Abbasi, A., Ahadi, M., Moallemi Rad, L. & Kobarfad, F. Assessment of the effects of intrastromal injection of adipose-derived stem cells in keratoconus patients. *Int J Ophthalmol* **16**, 863–870 (2023).

113. Alió Del Barrio, J. L. *et al.* Corneal Stroma Enhancement With Decellularized Stromal Laminas With or Without Stem Cell Recellularization for Advanced Keratoconus. *Am J Ophthalmol* **186**, 47–58 (2018).

114. Kaur, H. *et al.* Hydrogels as a Potential Biomaterial for Multimodal Therapeutic Applications. *Mol Pharm* **21**, 4827–4848 (2024).

115. Wang, Y. *et al.* Quercetin-Loaded Ceria Nanocomposite Potentiate Dual-Directional Immunoregulation via Macrophage Polarization against Periodontal Inflammation. *Small* **17**, 2101505 (2021).

116. Tan, Y.-Z. *et al.* Melatonin induces the rejuvenation of long-term ex vivo expanded periodontal ligament stem cells by modulating the autophagic process. *Stem Cell Res Ther.* **12**, 254 (2021).

117. Karoubi, G., Ormiston, M. L., Stewart, D. J. & Courtman, D. W. Single-cell hydrogel encapsulation for enhanced survival of human marrow stromal cells. *Biomaterials* **30**, 5445–5455 (2009).

118. de Vos, P., Lazarjani, H. A., Poncelet, D. & Faas, M. M. Polymers in cell encapsulation from an enveloped cell perspective. *Adv Drug Deliv Rev*. **67–68**, 15–34 (2014).

119. Gasperini, L., Mano, J. F. & Reis, R. L. Natural polymers for the microencapsulation of cells. *J R Soc Interface.* **11**, 20140817 (2014).

120. Hashemi, M. & Kalalinia, F. Application of encapsulation technology in stem cell therapy. *Life Sci.***143**, 139–146 (2015).

121. Nicodemus, G. D. & Bryant, S. J. Cell Encapsulation in Biodegradable Hydrogels for Tissue Engineering Applications. *Tissue Eng B, Reviews* **14**, 149 (2008).

122. de Vos, P., Andersson, A., Tam, S., Faas, M. & Halle, J. Advances and Barriers in Mammalian Cell Encapsulation for Treatment of Diabetes. *Immunol., Endo Metab Agents - Med Chem.* **6**, 139–153 (2006).

123. Zhao, Z. *et al.* Injectable Microfluidic Hydrogel Microspheres for Cell and Drug Delivery. *Adv Funct Mater.* **31**, 2103339 (2021).

124. Köster, S. *et al.* Drop-based microfluidic devices for encapsulation of single cells. *Lab on a chip* **8**, 1110–5 (2008).

125. Chen, J. *et al.* 3D bioprinted multiscale composite scaffolds based on gelatin methacryloyl (GelMA)/chitosan microspheres as a modular bioink for enhancing 3D neurite outgrowth and elongation. *J Colloid Interface Sci.***574**, 162–173 (2020).

126. Yue, J., Liu, Z., Wang, L., Wang, M. & Pan, G. Recent advances in bioactive hydrogel microspheres: Material engineering strategies and biomedical prospects. *Materials Today Bio* **31**, 101614 (2025).

127. Wang, R. *et al.* Adipose-derived stem cell/FGF19-loaded microfluidic hydrogel microspheres for synergistic restoration of critical ischemic limb. *Bioact Mater* **27**, 394–408 (2023).

128. Ichihara, Y. *et al.* Self-assembling peptide hydrogel enables instant epicardial coating of the heart with mesenchymal stromal cells for the treatment of heart failure. *Biomaterials* **154**, (2017).

129. Panda, N. *et al.* Improved conduction and increased cell retention in healed MI using mesenchymal stem cells suspended in alginate hydrogel. *J Interv Card Electrophysiol.* **41**, (2014).

130. Mathieu, E. *et al.* Intramyocardial Delivery of Mesenchymal Stem Cell-Seeded Hydrogel Preserves Cardiac Function and Attenuates Ventricular Remodeling after Myocardial Infarction. *PLOS ONE* **7**, e51991 (2012).

131. A5030-BULK_____SIAL_____.pdf.

132. Monette-Catafard, N. High-throughput cell encapsulation in monodisperse agarose microcapsules using a microfluidic device.

133. Benavente-Babace, A., Haase, K., Stewart, D. J. & Godin, M. Strategies for controlling egress of therapeutic cells from hydrogel microcapsules. *J Tissue Eng Regen Med.* **13**, 612–624 (2019).

134. Sia, S. K. & Whitesides, G. M. Microfluidic devices fabricated in Poly(dimethylsiloxane) for biological studies. *Electrophoresis* **24**, 3563–3576 (2003).

135. Duffy, D. C., McDonald, J. C., Schueller, O. J. A. & Whitesides, G. M. Rapid Prototyping of Microfluidic Systems in Poly(dimethylsiloxane). *Anal. Chem.* **70**, 4974–4984 (1998).

136. LIVE/DEAD Viability/Cytotoxicity Kit.

137. McLaughlin, S. *et al.* Injectable human recombinant collagen matrices limit adverse remodeling and improve cardiac function after myocardial infarction. *Nat Commun* **10**, 4866 (2019).

138. Aston, R., Sewell, K., Klein, T., Lawrie, G. & Grøndahl, L. Evaluation of the impact of freezing preparation techniques on the characterisation of alginate hydrogels by cryo-SEM. *Eur Polym J.***82**, 1–15 (2016).

139. Noudeh, G. D., Khazaeli, P., Mirzaei, S., Sharififar, F. & Nasrollahosaiani, S. Determination of the Toxicity Effect of Sorbitan Esters Surfactants Group on Biological Membrane. *J Biol Sci.* **9**, 423–430.

140. Hamilton, M., Harrington, S., Dhar, P. & Stehno-Bittel, L. Hyaluronic Acid Hydrogel Microspheres for Slow Release Stem Cell Delivery. *ACS Biomater. Sci. Eng.* **7**, 3754–3763 (2021).

141. Terrovitis, J. *et al.* Noninvasive Quantification and Optimization of Acute Cell Retention by In Vivo Positron Emission Tomography After Intramyocardial Cardiac-Derived Stem Cell Delivery. *J Am Coll Cardiol.***54**, 1619–1626 (2009).

142. Bonios, M. *et al.* Myocardial substrate and route of administration determine acute cardiac retention and lung bio-distribution of cardiosphere-derived cells. *J NuclCardiol.***18**, 443–450 (2011).

143. Kanda, P. *et al.* Deterministic paracrine repair of injured myocardium using microfluidic-based cocooning of heart explant-derived cells. *Biomaterials* **247**, 120010 (2020).

144. Blocki, A. *et al.* Microcapsules engineered to support mesenchymal stem cell (MSC) survival and proliferation enable long-term retention of MSCs in infarcted myocardium. *Biomaterials* **53**, 12–24 (2015).

145. Baldari, S. *et al.* Challenges and Strategies for Improving the Regenerative Effects of Mesenchymal Stromal Cell-Based Therapies. *Int J Mol Sci.* **18**, 2087 (2017).

146. Na, K.-S. *et al.* Effect of mesenchymal stem cells encapsulated within in situ forming PEG-collagen hydrogels on alkali-burned corneas in an ex vivo organ culture model. *Cytotherapy* **23**, 500–509 (2021).

147. Van den Bogerd, B., Dhubhghaill, S. N., Koppen, C., Tassignon, M.-J. & Zakaria, N. A review of the evidence for *in vivo* corneal endothelial regeneration. *Surv Ophthalmol.* **63**, 149–165 (2018).

148. Chandru, A. *et al.* Human Cadaveric Donor Cornea Derived Extra Cellular Matrix Microparticles for Minimally Invasive Healing/Regeneration of Corneal Wounds. *Biomolecules* **11**, 532 (2021).

149. Ibeas Moreno, E., Alonso, M. J. & Abbadessa, A. Intraocular injectable hydrogels for the delivery of cells and nanoparticles. *Mater Today Bio* **32**, 101767 (2025).

150. Ushikubo, F. Y. & Cunha, R. L. Stability mechanisms of liquid water-in-oil emulsions. *Food Hydrocolloids* **34**, 145–153 (2014).

151. Soucy, N. Hollow Hydrogel Cocoons for the Encapsulation of Therapeutic Cells Using a Microfluidic Platform.

152. *Surfactants: Chemistry, Interfacial Properties, Applications*. (2001).

153. Norn, V. *Emulsifiers in Food Technology: Second Edition*. 342 (2015). doi:10.1002/9781118921265.

154. Pham Le Khanh, H. *et al.* Comparative Investigation of Cellular Effects of Polyethylene Glycol (PEG) Derivatives. *Polymers (Basel)* **14**, 279 (2022).

155. Dutcher, M. *et al.* Encapsulating therapeutic cells in RGD-modified agarose microcapsules. *Biomed Mater.* **18**, (2023).

156. Na, J., Park, K. & Kwon, S. J. Single-Entity Electrochemistry in the Agarose Hydrogel: Observation of Enhanced Signal Uniformity and Signal-to-Noise Ratio. *Gels* **9**, 537 (2023).

157. Annabi, N. *et al.* Controlling the Porosity and Microarchitecture of Hydrogels for Tissue Engineering. *Tissue Eng B Rev* **16**, 371–383 (2010).

158. Brazdaru, L. *et al.* Structural and rheological properties of collagen hydrogels containing tannic acid and chlorhexidine digluconate intended for topical applications. *Comptes Rendus Chimie* **18**, 160–169 (2015).

159. Browning, M. B., Cereceres, S. N., Luong, P. T. & Cosgriff-Hernandez, E. M. Determination of the in vivo degradation mechanism of PEGDA hydrogels. *J Biomed Mater Res A* **102**, 4244–4251 (2014).

Supplementary Information

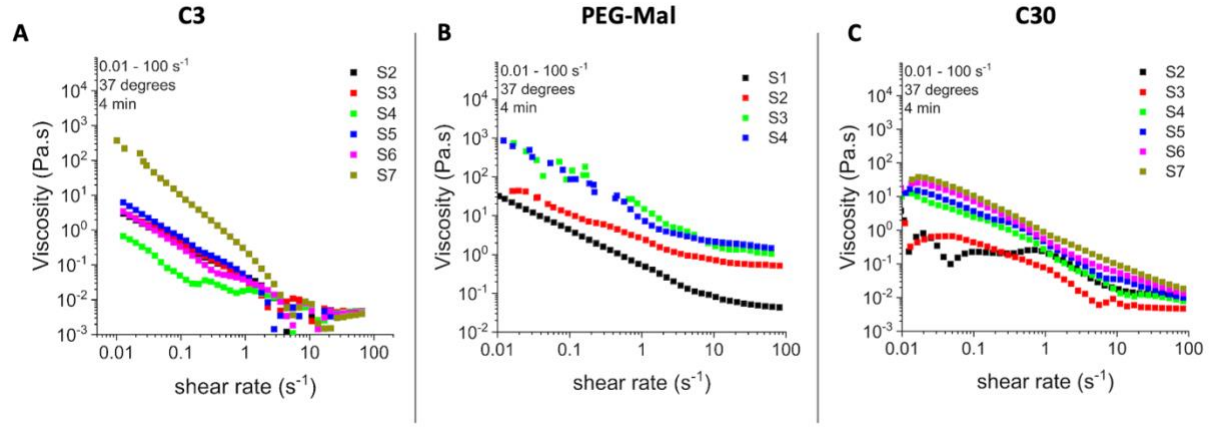

Supplementary Figure S1. Viscosities of different solutions (PEG-Mal, C3 and C30) at different shear rates. **A)** Graph showing the viscosity at different shear rates of increasing concentrations of C3 CLP (n=6). **B)** Viscosity at different shear rates of increasing concentrations of polyethylene glycol maleimide (PEG-Mal) solutions (n=4). **C)** Graph showing the viscosity of CLP C30 at different shear rates of increasing concentrations (n=6). Samples measured using Kinexus rheometer.

For C30 and C3: Concentrations refer to:

S2= 3mM; S3= 6mM; S4= 12mM; S5= 20mM; S6=30mM; S7= 40mM

For PEG-Mal: Concentrations refer to:

S1= 5mM; S2= 10 mM; S3= 15mM; S4= 20mM

Concentration range was chosen for each solution depending on the working concentration used to prepare hydrogels. The working concentration of PEG-Mal S1 shows higher viscosity than C3 and C30 in the whole shear range.

Table S1. Optimization of surfactant emulsion compositions for PEG-Mal solution and C30+PEG-Mal hydrogel formation. Various concentrations of Span 80 were tested to evaluate emulsion stability with PEG-Mal. Formulations were assessed based on emulsion stability, phase separation, and successful gelation to identify optimal conditions for microsphere generation.

PEG-Mal Concentration & Span80 in the emulsion	CLP Concentration	Gel formation (Yes/No)	Emulsion remained stable (Yes/No)	Additional Remarks
2mM PEG Span 1%	5 mM	Yes	No	Hydrogel melted around 6 hours after formation
2mM PEG Span 2%	5 mM	Yes	No	/
5mM PEG Span 1%	5 mM	No	No	/
5 mM PEG Span 2%	5 mM	Yes	Yes	Hydrogel formed- soft- could not be unmolded-
10 mM PEG Span 1%	5 mM	Yes	No	/
10 mM PEG Span 2%	5 mM	Yes	No	Elastic Hydrogel formed- elastic- could be molded with minimal shearing

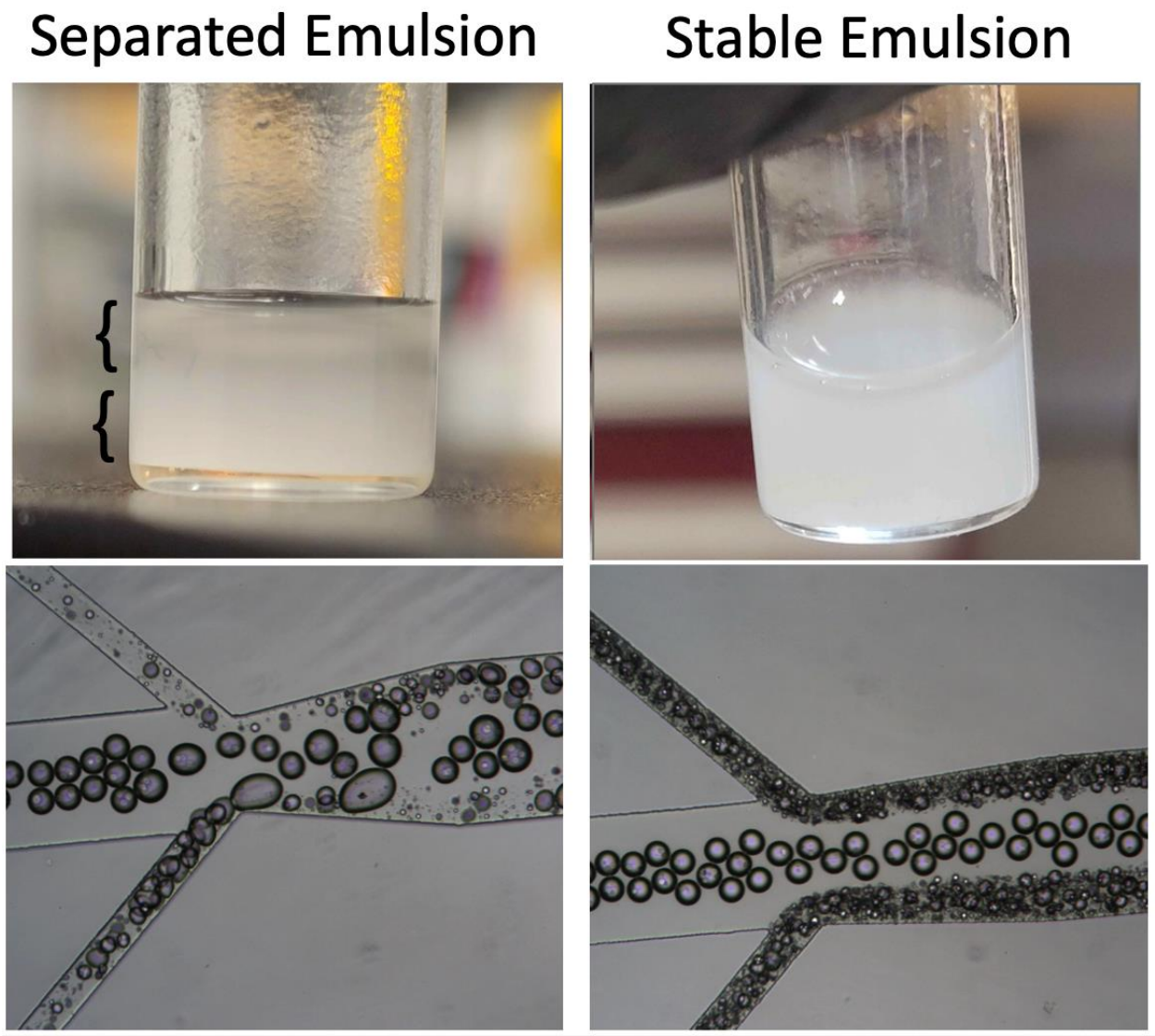

Supplementary Figure S2. **Comparison of unstable versus stable PEG-Mal/Span 80 emulsions and their effects on microfluidic flow behavior**. (**Left panel**) An unstable emulsion of PEG-Mal and Span 80 resulting in visible phase separation (top) and disrupted, uneven flow in the microfluidic inlets (bottom). (**Right panel**) A stable, homogeneous water-in-oil (W/O) emulsion of PEG-Mal and Span 80 (top) yielding a uniform and balanced flow in the microfluidic system (bottom), demonstrating the critical importance of emulsion stability for controlled microsphere generation. Stable W/O emulsion made with PEG-Mal and Mineral Oil with 2% Span 80 surfactant.

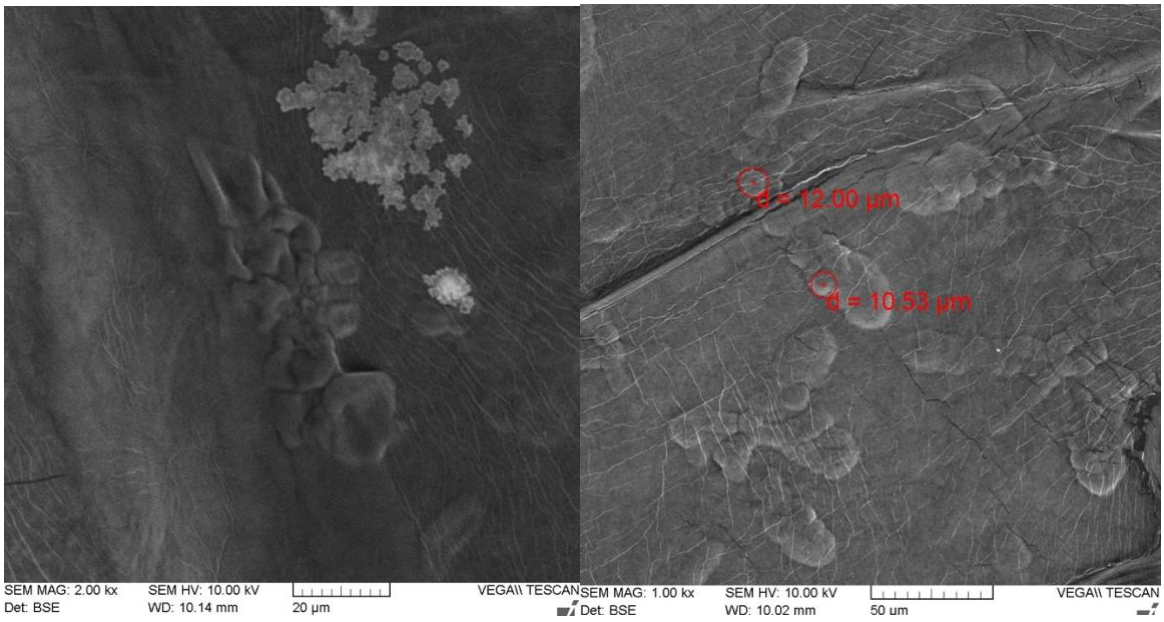

Supplementary Figure S3. SEM image of an agarose microsphere using the plasma-induced gold atoms sputter-coating process. This dry preparation approach did not preserve internal structure, revealing only the outer shell, unlike the cryo-SEM method which provided more detail.

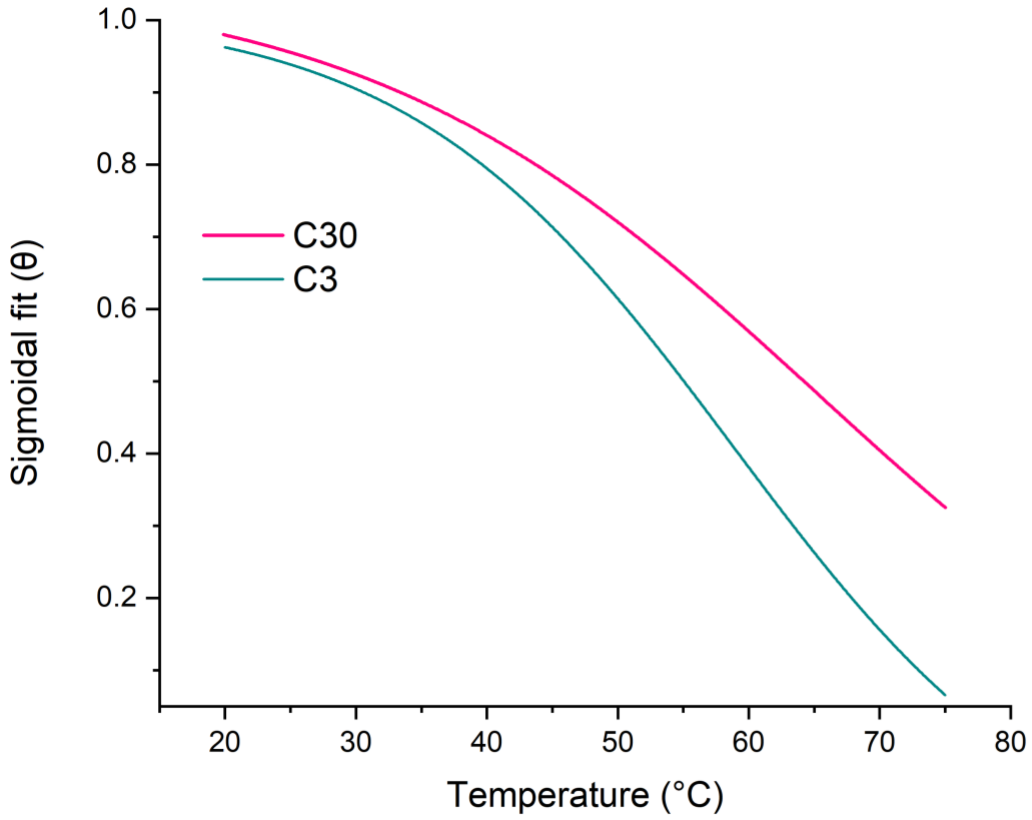

Supplementary Figure S4. Melting curves of C3, C30, and CLP peptides measured at 220 nm using circular dichroism spectroscopy (CD). Temperature scans were performed from 20°C to 75°C to assess peptide thermal stability. The resulting curves were fitted using a sigmoidal model with $R^2 > 0.99$. The midpoint of the thermal transition, melting temperature (Tm), reflects the thermal stability of each peptide which was reported in the table of melting temperatures, **Table 3**.

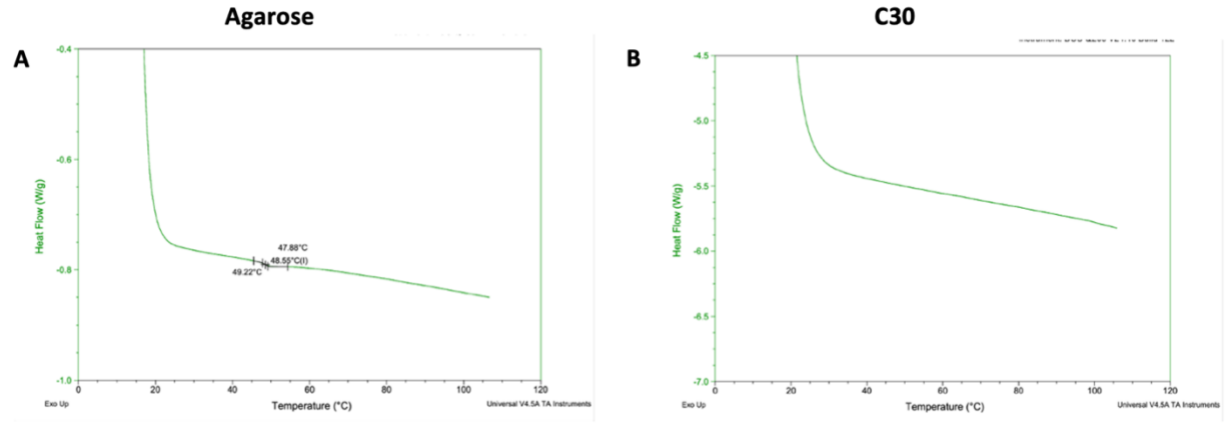

Supplementary Figure S5. Differential Scanning Calorimetry (DSC) thermograms of Agarose and C30 hydrogels. DSC analysis performed to evaluate the thermal stability and denaturation temperatures of the C30 peptide hydrogel and agarose (control).

DSC thermograph of agarose displays an endothermic transition between ~47.8°C and ~49.2°C**,** with a peak at approximately 48.5°C. This thermal event corresponds to the gel-sol transition (denaturation) of agarose, where the polymer network begins to disassemble upon heating. This is consistent with literature values, which report agarose melting transitions typically occurring in the 40–90°C range depending on concentration and gelling conditions. The distinct peak confirms thermal responsiveness and the defined gelation behavior of agarose.

The DSC curve for C30 lacks a distinct endothermic peak, displaying instead a gradual decrease in heat flow with increasing temperature. This suggests that no sharp thermal transition or denaturation event occurs within the tested range (up to ~100°C). The absence of a melting point indicates that the C30 hydrogel is thermally stable under physiological and moderately elevated temperatures. This thermal resilience is characteristic of synthetic peptide-based materials designed to maintain structural integrity for biomedical applications.

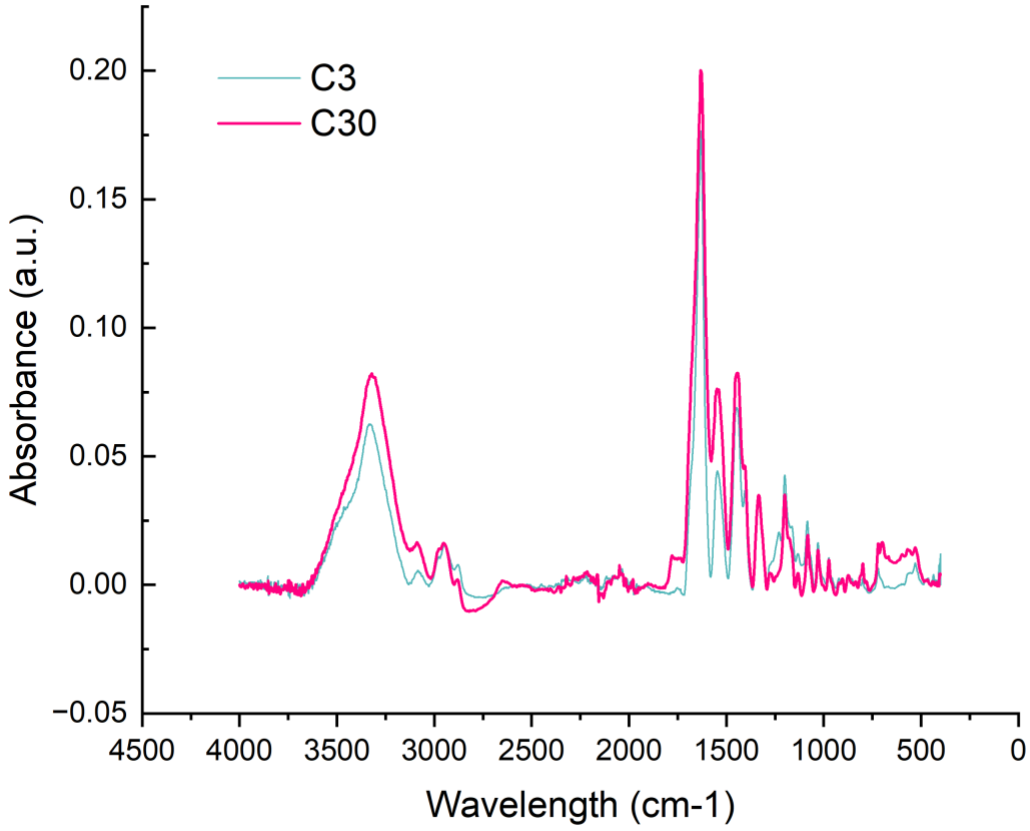

Supplementary Figure S6. Fourier-transform infrared (FTIR) spectrum of the C3 and C30 collagen-like peptides. The spectrum displays characteristic absorption bands associated with peptide secondary structures, including prominent peaks corresponding to Amide I (~1650 cm^{-1}), Amide II (~1550 cm^{-1}), and Amide III (~1240 cm^{-1}), as well as a broad O–H/N–H stretching band around 3300 cm^{-1}. These peaks confirm the presence of peptide bonds and hydrogen bonding interactions, supporting the structural identity and conformation of CLP.

Sample	Sequence	Molecular Weight (g/mol)	Residue Number	M+2H Ion	M+3H Ion
C3	NH_2-GCG**(POG)$_8$**GCG-OH	2591	30	1296.4	864.6

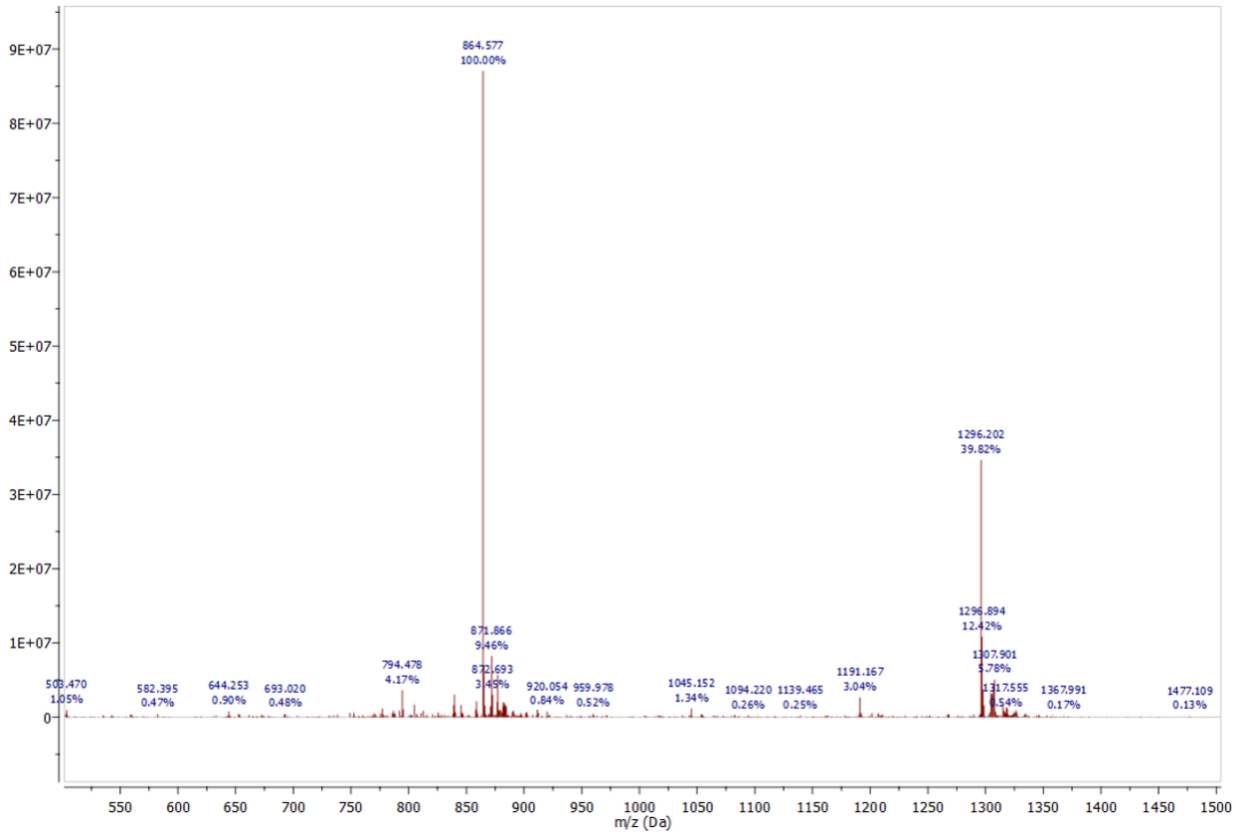

Supplementary Figure S7. Representative mass spectrometry data for CLP C3.

Sample	Sequence	Molecular Weight (g/mol)	Residue Number	M+2H Ion	M+3H Ion
C30	NH_2-GCG**(POG)$_{10}$**GCG-OH	3125	36	1563.7	1042.8

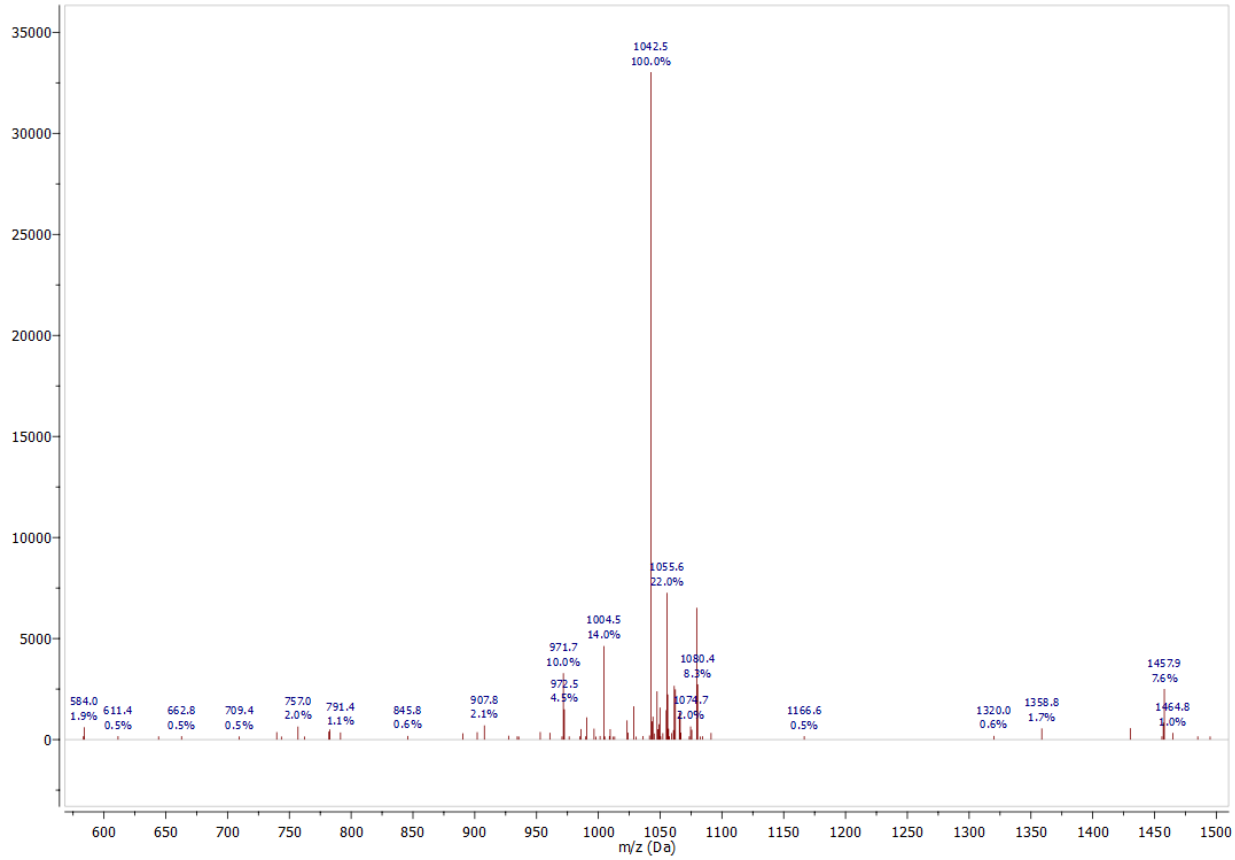

Supplementary Figure S8. Representative mass spectrometry data for CLP C30.

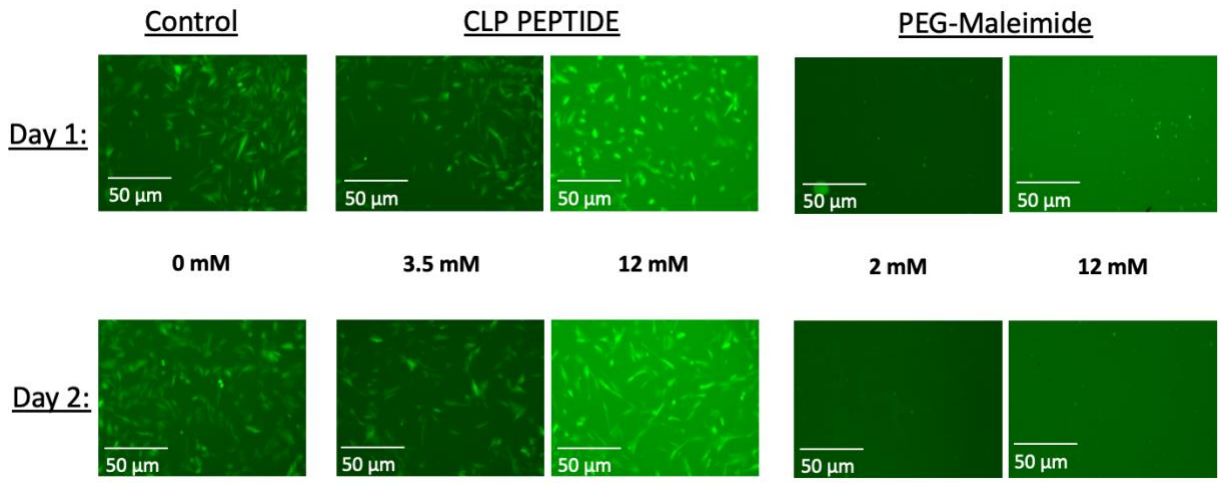

Supplementary Figure S9. GFP+Fibroblasts cultured with CLP and PEG-Mal at different concentrations to assess biocompatibility.